



Study on Effect of Spontaneous Polarizations on Electrical Properties of Ferroelectric/Polar Semiconductor Heterostructures

メタデータ	言語: English 出版者: 公開日: 2015-07-03 キーワード (Ja): キーワード (En): 作成者: 山田, 裕明 メールアドレス: 所属:
URL	https://doi.org/10.24729/00000150

**Study on Effect of Spontaneous Polarizations on
Electrical Properties of
Ferroelectric/Polar Semiconductor Heterostructures**

Hiroaki Yamada

February 2015

Doctoral Thesis at Osaka Prefecture University

Contents

Chapter 1: General Introduction

1.1 Field-effect control of carrier concentration.....	1
1.2 Ferroelectric field-effect	3
1.2.1 Ferroelectric gate field-effect transistors.....	3
1.2.2 Controlled-polarization-type field-effect transistors.....	4
1.2.3 Novel phenomena at ferroelectric interfaces.....	5
1.3 Abstract of thesis	8

Chapter 2: Fabrication and Electronic Transport Properties of CP-type FeFETs with YbMnO₃/ZnO Heterostructures

2.1 Introduction.....	16
2.2 Preparation and structural characterization of YbMnO ₃ /ZnO heterostructures.....	17
2.3 Electronic transport properties of YbMnO ₃ /ZnO heterostructures.....	21
2.4 Conclusions.....	29

Chapter 3: Effect of Ferroelectric Polarization on Electronic Transport Properties in Ferroelectric/Polar Semiconductor Heterostructures

3.1 Introduction.....	32
3.2 Experimental procedures.....	33
3.3 Results and discussion.....	34
3.3.1 Effect of ferroelectric domain structures in electronic transport properties of poly(vinylidene fluoride-tetrafluoroethylene)/ZnO heterostructures.....	34

3.3.2 Electrical and electronic transport properties of poly(vinylidene fluoride-tetrafluoroethylene)/ZnO heterostructures with various channel thicknesses.....	42
3.4 Conclusions.....	58

Chapter 4: Effect of Spontaneous Polarization of Polar Semiconductor on Electrical Properties of Poly(vinylidene fluoride-trifluoroethylene)/ZnO Heterostructures

4.1 Introduction.....	62
4.2 Experimental procedures.....	62
4.3 Results and discussion.....	63
4.3.1 Electrical properties of poly(vinylidene fluoride-trifluoroethylene)/O- and Zn-polar ZnO heterostructures.....	63
4.3.2 Analysis of band alignments of heterostructures with poly(vinylidene fluoride-trifluoroethylene)/O- and Zn-polar ZnO heterostructures.....	68
4.4 Conclusions.....	74

Chapter 5: Crystal Growth of (111) (Ba_{1-x}Ca_x)TiO₃ on (000 $\bar{1}$) ZnO Substrates for Lattice Matched Heterostructures with Ferroelectrics and Polar Semiconductors

5.1 Introduction.....	76
5.2 Experimental procedures.....	77
5.3 Results and discussion.....	78
5.4 Conclusions.....	86

Chapter 6: Summary..... 90

Acknowledgements..... 93

Chapter 1: General Introduction

1.1 Field-effect control of carrier concentration

Recently, surface and interface phenomena have attracted much attention because of the ability to distinguish physical properties from bulk materials. In actual devices, the ability to control the carrier concentration is an important factor that is considered when using these distinguishing properties. The field effect is an effective tool that is employed for carrier doping at heterointerfaces because it can vary the carrier concentration continuously and independently. There have been significant developments in field-effect technologies in the field of Si metal-oxide-semiconductor field-effect-transistors (MOSFETs). The main advantage of Si MOSFETs is the clean and comfortable interface formation with SiO₂. Moreover, the effects of the electrostatic field on the carrier transport in Si MOSFETs have been extensively examined. S. Takagi et al. proposed three scattering mechanisms, namely Coulomb (impurity) scattering, phonon scattering, and surface-roughness scattering. Coulomb scattering was shown to decrease in the presence of strong electric fields, while surface scattering degrades the carrier mobility in stronger electric fields [1–3]. These principles were applied to other material systems such as the high-k materials of the hafnium family and composite semiconductors such as GaAs [4–7]. Field-effect control at heterojunctions with compound semiconductors enables us to modulate two-dimensional gas (2DEG), and has contributed to the development of high-electron-mobility transistors (HEMTs) [8]. Al_xGa_{1-x}As/GaAs HEMT uses the modulation doping system, which triggers the flow of electrons in Al_xGa_{1-x}As to GaAs using the potential differences in Al_xGa_{1-x}As/GaAs. Using the modulation doping technique, high electron-mobility values exceeding $10^6 \text{ cm}^2\text{V}^{-1}\text{s}^{-1}$ are found to be compatible with the

interface carrier at around 10^{12} cm^{-2} .

The use of the spontaneous (piezoelectric) polarization charge was proposed as a new carrier-doping method in HEMT devices that have $\text{Al}_x\text{Ga}_{1-x}\text{N}/\text{GaN}$. The discontinuity of polarizations in $\text{Al}_x\text{Ga}_{1-x}\text{N}/\text{GaN}$ results in a carrier generation of 10^{13} cm^{-2} . Polarization-mediated 2DEGs, which were obtained by oxide heterostructures with the ZnO-related systems, were also realized, and they achieved high electron-mobility values that were approximately $10^6 \text{ cm}^2\text{V}^{-1}\text{s}^{-1}$, which are close to the values obtained for other HEMT systems [9, 10]. For these systems, to realize the precise control of interface electrical properties, the relationship between the carrier concentration in 2DEG and the difference in the polarization charge at the heterointerfaces was discussed.

Recently, heterointerfaces with oxide materials have attracted significant interest because of their novel capabilities. Developments in the area of thin-film technologies such as molecular-beam epitaxy enable us to fabricate epitaxial films with atomic-level control and to understand the emerging properties such as metallic conduction at insulator interfaces [11], the tunable spin-orbit interaction through external electric fields [12], and the formation of low-dimensional electronic structures [13–15]. These properties can be controlled via carrier doping based on their chemical compositions, the carrier modulation based on the field effect, and the strains based on the lattice mismatches with substrates. Gate-stacking systems with ionic liquids, organic materials, correlate oxides, and ferroelectrics have also attracted some interest. The charge injection and transfer at the inorganic-organic interface [16, 17], as well as the control of the Mott transition [17, 18] and superconducting transition temperatures using the electric double-layer transistor (EDLT) [19] have been reported. EDLTs, which are field-effect devices with ionic-liquid gates, have been commonly used in studies involving interfacial physical properties, and have the advantage of realizing high carrier doping of up to 10^{15} cm^{-2} . Ferroelectrics are

also an attractive material in this field because they have large and switchable spontaneous polarizations. Typical ferroelectrics such as $\text{Pb}(\text{Zr,Ti})\text{O}_3$, BaTiO_3 (BTO), and BiFeO_3 exhibit polarization charges that range from 10 to $100 \mu\text{C}/\text{cm}^2$ [20–26], which corresponds to the surface charges of EDLTs. These polarizations can be controlled at relatively low electric fields below $100 \text{ kV}/\text{cm}$. These ferroelectric properties enable the development of electronic devices using ferroelectric polarization-mediated interfaces. FETs with ferroelectric gate stacks are believed to be among the next generation of nonvolatile memories.

1.2 Ferroelectric field-effect

1.2.1 Ferroelectric gate field-effect transistors

Ferroelectric gate FETs (FeFETs) have been studied from the perspective of practical applications of nonvolatile memory because of their nondestructive readout, high-speed operation, and low power consumption [27–34]. FeFETs operate by performing carrier modulation in channel semiconductors using polarization switching. Many challenges were faced in order to enable FeFETs to obtain high-quality ferroelectric gate layers on Si and other conventional semiconductors. However, oxidation and interdiffusion at the heterointerfaces degrade the ferroelectricity, and the devices exhibited poor retention and endurance. To overcome these problems, Sakai et al. proposed the use of a buffer layer with high- k dielectrics [27]. They succeeded in obtaining a retention time of more than 10^5 s. Kato et al. proposed metal-ferroelectric-semiconductor (MFS) structures with a highly crystalline ferroelectric using epitaxial oxide heterostructures [28]. FeFETs with $\text{ZnO}/\text{Pb}(\text{Zr,Ti})\text{O}_3/\text{SrRuO}_3$ heterostructures achieved a large ON/OFF ratio of 10^5 and retention time over 10^5 s. To realize the practical use of FeFETs as nonvolatile memories, many studies have been performed, such as a low-temperature fabrication process using

organic ferroelectrics [29], the use of FeFETs with a total solution process [31], the use of a sub-100-nm channel length FeFET [32], and the demonstration of NOR and NAND memory cells using FeFETs [33, 34]. These devices were successfully operated by employing polarization switching of the ferroelectric gate. However, FeFETs were found to have the low field-effect mobility values. Kaneko et al. reported a memory cell composed of a FeFET and an insulator- (SiN_x) gate FET. In that study, the field-effect mobilities were 25 and 0.1 in the FET and FeFET, respectively. The authors reported that the former value corresponded to the result of the Hall-effect measurement of ZnO films ($26 \text{ cm}^2/\text{Vs}$), although the latter was degraded by interface-roughness scattering. The results revealed two problems that are associated with FeFETs. One is the degradation of the mobility because of the higher field effect, which is caused by the large polarization. The second is the possibility that the calculation method includes an incorrect assumption. The field-effect mobility is usually calculated using the polarization-voltage (P - V) curve because ferroelectrics have nonlinear dielectric (capacitance) characteristics when a voltage is applied. This method assumes that ferroelectric polarization completely induces the carriers at the heterointerfaces, although the carrier concentration of the channel has a large charge mismatch with the ferroelectric polarization charge. Therefore, to understand electron transport in FeFETs, there is a need for a detailed discussion regarding the relationship between ferroelectric polarization and interface carriers, as well as an experimental approach involving techniques such as Hall-effect measurements.

1.2.2 Controlled-polarization-type field-effect transistors

Fukushima et al. proposed the use of the heterointerface of ferroelectric and polar semiconductors for FeFETs, which is called controlled-polarization (CP)-type FeFETs [35, 36]. The interaction between the polarizations of the gate ferroelectrics and polar

semiconductors is expected. When the polarizations align head-to-head, electrons that correspond to the sum of the polarizations are induced at the interface. Therefore, head-to-head polarizations increase the ON current. When the polarizations are aligned in the same direction, the polar semiconductor should be depleted. Then, it is expected that the spontaneous polarization of the polar semiconductor will reduce the depolarization field because it compensates for the mismatched charge at the interface. It has been demonstrated the non-volatile memory operation of CP-type FeFETs composed of the hexagonal ferroelectrics of RMnO_3 (R: Y, Yb) and the polar semiconductors of ZnO .

1.2.3 Novel phenomena at ferroelectric interfaces

Recent developments regarding the epitaxial growth techniques of oxides have enabled the formation of high-quality ferroelectric thin films. These epitaxial films generate novel functional properties such as the modulation of the interface electrical and magnetic properties, the anomalous increase in the polarization, and resistive switching. This functionality arises from the large and switchable polarization of ferroelectrics. Ahn et al. reported the modulation of the critical temperature of the high-temperature superconductor $\text{GdBa}_2\text{Cu}_3\text{CuO}_{7-x}$ using the field-effect through the polarization of $\text{Pb}(\text{Zr}, \text{Ti})\text{O}_3$ [37]. There was a 7 K change in the critical temperature obtained, which is larger than that of the electrostatic field modulation obtained using dielectric polarization (~ 2 K) [38]. Stolichnov et al. reported the nonvolatile control of ferromagnetism in $(\text{Ga}, \text{Mn})\text{As}$ with the ferroelectric gate [39]. They demonstrated that the ferromagnetic-paramagnetic phase transition can be modulated by the polarization of the ferroelectric polymer of poly(vinylidene fluoride-trifluoroethylene) (P(VDF-TrFE)). These results indicate that ferroelectrics possess significant potential for the modulation effect of physical properties at heterointerfaces.

Based on the ferroelectric properties, changes in the physical properties at heterointerfaces were also observed. Many studies have focused on the enhancement of ferroelectricity using the epitaxial strain [26, 40–42]. Choi et al. demonstrated significant increases in the ferroelectric transition temperature up to 500°C and at least 250% in the remnant polarization for BTO thin films. This was realized by using the coherent compressive strain ($\sim 1.7\%$) of DyScO₃ substrates. The compressive strain from the substrates stabilizes the thermodynamic energy of the ferroelectric phase and enhances the tetragonality of ferroelectric crystals; this results in a highly ferroelectric transition temperature and anomalous polarization [24–26, 43, and 44]. These reports indicate the possibility of using ferroelectric thin films that have thicknesses of several nanometers, which generate quantum-size effect.

On the other hand, it is known that there are degradations of the ferroelectricity at heterointerfaces. Undesirable factors such as dangling bonds, incoherent strain, and charge mismatches should be reduced by performing local modulation at the heterointerfaces. Several reports have denoted the interface structural modulation such as local-ion pinning by oxygen vacancies and the zigzag-shaped polarization domains for charge compensation using transmission electron microscopy and angle-resolved X-ray photoelectron spectroscopy (XPS) [45–48]. However, the origins of the degradation effects are underspecified because of the coexistence of undesirable factors such as a variety of defects, incoherent deformation caused by strains, and imperfect charge screening at heterointerfaces. Therefore, to understand the effect of polarization on the electrical properties, including these local effects, there is a need for careful discussions from a quantitative perspective, which includes these undesirable factors.

In some cases, the modulation effects of ferroelectric polarization are exhibited by changes in the resistivity. Two types of devices were demonstrated. Ferroelectric diodes are

among the novel ferroelectric nonvolatile memory devices that utilize changes in the Schottky barrier height at the heterointerfaces depending on the direction of ferroelectric polarization [49, 50]. These phenomena originate from the formation of the space charge region at the interfaces, as well as the transfer of mobile ions or defects such as oxygen vacancies. Ferroelectric tunneling junctions (FTJs) are another type of novel ferroelectric nonvolatile memory devices. FTJs are composed of ultrathin ferroelectrics, which enable direct tunneling conduction, and asymmetric heterointerfaces with electrodes [51–56]. The principles of the resistive changes in the FTJs are proposed as the electrostatic-field effect, microscopic interface effect with displacement of ions, and strain effect [57–59]. The significant FTJ-based reports have focused on the strained BiFeO₃ and the field-effect at the heterojunction with semiconductors [53, 54]. Other interesting reports are multi-level operations that used the multiferroic properties and the polarization domain structures [55, 56]. These devices are very sensitive to the interface phenomena because operation mechanisms originate from the transfer of defects and ions, as well as modulations of the interface electrostatic potential, which is generated close to interfaces, and is caused by ferroelectric polarization. Therefore, in order to develop novel nonvolatile memory elements, it is important to understand the mechanism related to the ferroelectric interface phenomena.

The ferroelectric field-effect has good potential for the control of physical properties such as channel conductivity, magnetic properties, ion transfer, and electrostatic potential. For investigations into the novel physical properties and the practical use of ferroelectrics, it is important to have a good understanding of interface phenomena such as carrier modulation and compensation effects caused by ferroelectric polarization, local structural modification with the ferroelectric domain, and the polarization mediated field-effect at the ferroelectric-semiconductor interface.

1.3 Abstract of thesis

In this study, field effects caused by the spontaneous polarizations of ferroelectrics and polar semiconductors were discussed. The heterostructures comprising a polar ZnO semiconductor and various ferroelectrics of $(\text{Ba}_{1-x}\text{Ca}_x)\text{TiO}_3$ (BCT), YbMnO_3 , poly(vinylidene fluoride-tetrafluoroethylene) (P(VDF-TeFE)), and P(VDF-TrFE) were fabricated, and the electrical properties of these heterostructures were investigated.

This thesis is composed of six chapters.

In chapter 2, electronic transport properties of ferroelectric/polar semiconductor heterostructures were discussed. Hexagonal ferroelectrics of YbMnO_3 were grown on ZnO thin films using pulsed laser deposition (PLD) techniques. The heterostructures were processed into Hall bar structures in order to better understand details of the conduction mechanism at ferroelectric/polar semiconductor interfaces. The Hall-effect measurements of ZnO thin films and CP-type FeFETs with $\text{YbMnO}_3/\text{ZnO}$ heterostructures were carried out at various temperatures ranging from 80 to 300 K. The results show clear decreases in the carrier concentration and electron mobility caused by the deposition of YbMnO_3 . The electronic properties were analyzed using various scattering mechanisms including polar-optical phonon scattering, acoustic-phonon scattering caused by the deformation potential and the piezoelectric potential, ionized-impurity scattering, and grain-boundary scattering. From the analysis, it was determined that the dominant scattering factor changed from grain-boundary to ionized-impurity scattering. As a result, the origin of the distinct changes in the electronic transport properties is attributed to a partial depletion of ZnO, which was induced by the spontaneous polarization of YbMnO_3 .

In chapter 3, the effect of ferroelectric polarization on the electronic transport properties was investigated using P(VDF-TeFE)/ZnO Hall-bar structures with gate-electrode stacks. Moreover, to obtain good operating properties, optimization of the

deposition condition of ZnO, structural optimization, and the adaptation of the organic ferroelectric, P(VDF-TeFE), were performed. Based on the results obtained in chapter 2, the effect of the ferroelectric polarization domain was considered. Therefore, Hall-effect measurements of the P(VDF-TeFE)/ZnO heterostructures using the poling treatments were performed to discuss the effect of the ferroelectric domain structure on the electronic transport property in CP-type FeFETs.

In chapter 4, the effect of spontaneous polarization of polar semiconductors on the electrical properties and the charge matching mechanism at ferroelectric/polar semiconductor heterointerfaces were discussed. Heterostructures that are composed of P(VDF-TrFE) and ZnO with different crystallographic polarities of O- and Zn-polar ZnO were fabricated. First, the electrical properties of P(VDF-TrFE)/O- and Zn-polar ZnO were investigated. P(VDF-TrFE)/O- and Zn-polar ZnO exhibit clear differences in the depletion regions of the capacitance-voltage and the P - V characteristics. XPS using a synchrotron radiation beam was performed to analyze the electrical properties from the perspective of the band configuration. The XPS spectra indicated that the valence band maximum of P(VDF-TrFE) is 2.9 and 2.7 eV higher than Zn- and O-polar ZnO, respectively. Thus, staggered band configurations with large valence band offsets were shown in both P(VDF-TrFE)/O- and Zn-polar ZnO, and the spontaneous polarization of ZnO is less effective on the valence band offset. Moreover, the presence of a large number of trapping states is inferred from the thermal-activated current characteristics. Based on the results obtained, the relationships between the electrical properties, the band configuration, and charge-compensation mechanism of P(VDF-TrFE)/ZnO were discussed.

Chapter 5 focuses on the fabrication of ferroelectric/polar semiconductor heterostructures with small lattice misfits, where they have few defects, dislocations, and stains. The epitaxial growth of perovskite ferroelectrics of BCT thin films on ZnO was

investigated using a PLD system. The growth of (111) BCT film is expected because of lattice matching to ZnO substrate with the epitaxial relationship of $(111)[110]\text{BCT} \parallel (000\bar{1})[10\bar{1}0]\text{ZnO}$. However, (001) BCT thin films were only grown on ZnO. The $(\sqrt{3} \times \sqrt{3})\text{R}30^\circ$ reconstructed surface of ZnO was applied to reduce the charge mismatch at the BCT/ZnO interface. As a result, using the reconstruction surface, (111) BCT thin films were successfully grown on ZnO with an in-plane epitaxial relationship of $[110]\text{BCT} \parallel [10\bar{1}0]\text{ZnO}$.

Chapter 6 summarizes the main results and presents the conclusions of this thesis.

References

- [1] S. Takagi, A. Toriumi, M. Iwase, and H. Tango, IEEE trans. Electron Devices **41**, 2357 (1994).
- [2] S. Takagi, A. Toriumi, M. Iwase, and H. Tango, IEEE trans. Electron Devices **41**, 2363 (1994).
- [3] Y. Zhao, H. Matsumoto, T. Sato, S. Koyama, M. Takenaka, and S. Takagi, IEEE trans. Electron Devices **57**, 2057 (2010).
- [4] R. Chau, J. Brask, S. Datta, G. Dewey, M. Doczy, B. Doyle, J. Kavalieros, B. Jin, M. Metz, A. Majumdar, and M. Radosavljevic, Microelectronic Engineering **80**, 1 (2005).
- [5] M. Yokoyama, T. Yasuda, H. Takagi, N. Miyata, Y. Urabe, H. Ishii, H. Yamada, N. Fukuhara, M. Hata, M. Sugiyama, Y. Nakano, M. Takenaka, and S. Takagi, Appl. Phys. Lett. **96**, 142106 (2010).
- [6] Y. Xuan, Y. Q. Wu, H. C. Lin, T. Shen, and P. D. Ye, IEEE trans. **28**, 935 (2007).
- [7] V. Tilak, K. Matocha, and G. Dunne, IEEE trans. Electron Devices **54**, 2823 (2007).
- [8] T. Mimura, S. Hiyamizu, T. Fujii, and K. Nanbu, Jpn. J. Appl. Phys. **19**, L225 (1980).
- [9] T. Eda Hiro, N. Fujimura, and T. Ito, J. Appl. Phys. **93**, 7673 (2003).
- [10] J. Falson, D. Maryenko, Y. Kozuka, A. Tsukazaki, and M. Kawasaki, Appl. Phys. Express **4**, 091101 (2011).
- [11] A. Ohtomo and H. Y. Hwang, Nature **427**, 423 (2004).
- [12] H. Yuan, M. S. Bahramy, K. Morimoto, S. Wu, K. Nomura, B. -J. Yang, H. Shimotani, R. Suzuki, M. Toh, C. Kloc, X. Xu, R. Arita, N. Nagaosa, and Y. Iwasa, Nature Physics **9**, 563 (2013).
- [13] A. Tsukazaki, S. Akasaka, K. Nakahara, Y. Ohno, D. Maryenko, A. Ohtomo, and M. Kawasaki, Nature Mater. **9**, 889 (2010).
- [14] G. Cheng, P. F. Siles, F. Bi, C. Cen, D. F. Bogorin, C. W. Bark, C. M. Folkman, J. -W.

- Park, C. -B. Eom, G. M. Ribeiro, and J. Levy, *Nature Nanotechnology* **6**, 343 (2011).
- [15] H. Ohta, S. Kim, Y. Mune, T. Mizoguchi, K. Nomura, S. Ohta, T. Nomura, Y. Nakanishi, Y. Ikuhara, M. Hirano, H. Hosono, and K. Koumoto, *Nature Mater.* **6**, 129 (2007).
- [16] Y. Yuan, T. J. Reece, P. Sharma, S. Poddar, S. Ducharme, A. Gruverman, Y. Yang, and J. Huang, *Nature Mater.* **10**, 296 (2011).
- [17] C. H. Ahn, A. Bhattacharya, M. D. Ventra, J. N. Eckstein, C. D. Frisbie, M. E. Gershenson, A. M. Goldman, I. H. Inoue, J. Mannhart, A. J. Millis, A. F. Morpurgo, D. Natelson, and J. -M. Triscone, *Rev. Mod. Phys.* **78**, 1185 (2006).
- [18] S. Okamoto and A. J. Millis, *Nature* **428**, 630 (2004).
- [19] K. Ueno, S. Nakamura, H. Shimotani, A. Ohtomo, N. Kimura, T. Nojima, H. Aoki, Y. Iwasa, and M. Kawasaki, *Nature Mater.* **7**, 885 (2008).
- [20] W. L. Warren, D. Dimos, B. A. Tuttle, G. E. Pike, R. W. Schwartz, P. J. Clews, and D. C. McIntyre, *J. Appl. Phys.* **77**, 6695 (1995).
- [21] H. Funakubo, T. Watanabe, H. Morioka, A. Nagai, T. Oikawa, M. Suzuki, H. Uchida, S. Kouda, and K. Saito, *Materials Science and Engineering: B* **118**, 23 (2005).
- [22] X. X. Wang, X. G. Tang, and H. L. W. Chan, *Appl. Phys. Lett.* **85**, 91 (2004).
- [23] D. J. Kim, J. Y. Jo, Y. S. Kim, Y. J. Chang, J. S. Lee, J. -G. Yoon, T. K. Song, and T. W. Noh, *Phys. Rev. Lett.* **95**, 237602 (2005).
- [24] K. Y. Yun, D. Ricinschi, T. Kanashima, M. Noda, and M. Okuyama, *Jpn. J. Appl. Phys.* **43**, L647 (2004).
- [25] J. Yan, M. Gomi, T. Yokota, and H. Song, *Appl. Phys. Lett.* **102**, 222906 (2013).
- [26] K. J. Choi, M. Biegalski, Y. L. Li, A. Sharan, J. Schubert, R. Uecker, P. Reiche, Y. B. Chen, X. Q. Pan, V. Gopalan, L. -Q. Chen, D. G. Schlom, and C. B. Eom, *Science* **306**, 1005 (2004).

- [27] S. Sakai, R. Ilangoan, and M. Takahashi, *Jpn. J. Appl. Phys.* **43**, 7876 (2004).
- [28] Y. Kato, Y. Kaneko, H. Tanaka, and Y. Shimada, *Jpn. J. Appl. Phys.* **47**, 2719 (2008).
- [29] S. Fujisaki, H. Ishiwara, and Y. Fujisaki, *Appl. Phys. Express* **1**, 081801 (2008).
- [30] T. Miyasako, M. Senoo, and E. Tokumitsu, *Appl. Phys. Lett.* **86**, 162902 (2005).
- [31] T. Miyasako, B. N. Q. Trinh, M. Onoue, T. Kaneda, P. T. Tue, E. Tokumitsu, and T. Shimoda, *Jpn. J. Appl. Phys.* **50**, 04DD09 (2011).
- [32] Y. Kaneko, Y. Nishitani, M. Ueda, E. Tokumitsu, and E. Fujii, *Appl. Phys. Lett.* **99**, 182902 (2011).
- [33] Y. Kaneko, H. Tanaka, and Y. Kato, *Jpn. J. Appl. Phys.* **48**, 09KA19 (2009).
- [34] T. Hatanaka, M. Takahashi, S. Sakai, and K. Takeuchi, *IEICE Trans. electron.* **94**, 539 (2011).
- [35] T. Fukushima, T. Yoshimura, K. Masuko, K. Maeda, A. Ashida, and N. Fujimura, *Jpn. J. Appl. Phys.* **47**, 8874 (2008).
- [36] T. Fukushima, K. Maeda, T. Yoshimura, A. Ashida, and N. Fujimura, *Jpn. J. Appl. Phys.* **50**, 04DD16 (2011).
- [37] C. H. Ahn, S. Gariglio, P. Paruch, T. Tybell, L. Antognazza, and J.-M. Triscone, *Science* **284**, 1152 (1999).
- [38] X. X. Xi, Q. Li, C. Doughty, C. Kwon, S. Bhattacharya, A. T. Findikoglu, and T. Venkatesan, *Appl. Phys. Lett.* **59**, 3470 (1991).
- [39] I. Stolichnov, S. W. E. Rieker, H. J. Trodahl, N. Setter, A. W. Rushforth, K. W. Edmonds, R. P. Campion, C. T. Foxon, B. L. Gallagher, and T. Jungwirth, *Nature Mater.* **7**, 464 (2008).
- [40] N. A. Pertsev, A. G. Zembilgotov, and A. K. Tagantsev, *Phys. Rev. Lett.* **80**, 1988 (1998).
- [41] V. Nagarajan, I. G. Jenkins, S. P. Alpay, H. Li, S. Aggarwal, L. S.- Riba, A. L.

- Roytburd, and R. Ramesh, J. Appl. Phys. **86**, 595 (1999).
- [42] H. Morioka, G. Asano, T. Oikawa, H. Funakubo, and K. Saito, Appl. Phys. Lett. **82**, 4761 (2003).
- [43] D. Ricinschi, K.-Y. Yun, and M. Okuyama, J. Phys.: Condens. Matter **18**, L97 (2006).
- [44] H. Bea, B. Dupe, S. Fusil, R. Mattana, E. Jacquet, B. W.-. Fonrose, F. Wilhelm, A. Rogalev, S. Petit, V. Cros, A. Anane, F. Petroff, K. Bouzehouane, G. Geneste, B. Dkhil, S. Lisenkov, I. Ponomareva, L. Bellaiche, M. Bibes, and A. Barthelemy, Phys. Rev. Lett. **102**, 217603 (2009).
- [45] C. H. Park and D. J. Chadi, Phys. Rev. B **57**, R13961 (1998).
- [46] J. S. Speck, A. C. Daykin, A. Seifert, A. E. Romanov, and W. Pompe, J. Appl. Phys. **78**, 1696 (1995).
- [47] Y. -M. Kim, A. Morozovska, E. Eliseev, M. P. Oxley, R. Mishra, S. M. Selbach, T. Grande, S. T. Pantelides, S. V. Kalinin, and A. Y. Borisevich, Nature Mater. **13**, 1019 (2014).
- [48] H. Xu, X. Liu, X. Fang, H. Xie, G. Li, X. Meng, J. Sun, and J. Chu, J. Appl. Phys. **105**, 034107 (2009).
- [49] A. Tsurumaki, H. Yamada, and A. Sawa, Adv. Funct. Mater. **22**, 1040 (2012).
- [50] D. Lee, S. H. Baek, T. H. Kim, J. -G. Yoon, C. M. Folkman, C. B. Eom, and T. W. Noh, Phys. Rev. B **84**, 125305 (2011).
- [51] J. R. Contreras, H. Kohlstedt, U. Poppe, R. Waser, C. Buchal, and N. A. Pertsev, Appl. Phys. Lett. **83**, 4595 (2003).
- [52] M. Hambe, A. Petraru, N. A. Pertsev, P. Munroe, V. Nagarajan, and H. Kohlstedt, Adv. Funct. Mater. **20**, 2436 (2010).
- [53] Z. Wen, C. Li, D. Wu, A. Li, and N. Ming, Nature Mater. **12**, 617 (2013).
- [54] H. Yamada, V. Garcia, S. Fusil, S. Boyn, M. Marinova, A. Gloter, S. Xavier, J. Grollier,

- E. Jacquet, C. Carretero, C. Deranlot, M. Bibes, and A. Barthelemy, ACS Nano **7**, 5385 (2013).
- [55] A. Chanthbouala, V. Garcia, R. O. Cherifi, K. Bouzehouane, S. Fusil, X. Moya, S. Xavier, H. Yamada, C. Deranlot, N. D. Mathur, M. Bibes, A. Barthelemy, and J. Grollier, Nature Mater. **11**, 860 (2012).
- [56] D. J. Kim, H. Lu, S. Ryu, C.-W. Bark, C.-B. Eom, E. Y. Tsymbal, and A. Gruverman, Nano Lett. **12**, 5697 (2012).
- [57] E. Y. Tsymbal and H. Kohlstedt, Science **313**, 181 (2006).
- [58] M.Y. Zhuravlev, R. F. Sabirianov, S. S. Jaswal, and E.Y. Tsymbal, Phys. Rev. Lett. **94**, 246802 (2005).
- [59] H. Kohlstedt, N. A. Pertsev, J. R. Contreras, and R. Waser, Phys. Rev. B **72**, 125341 (2005).

Chapter 2: Fabrication and Electronic Transport Properties of CP-type FeFETs with YbMnO₃/ZnO Heterostructures

2.1 Introduction

The CP-type FeFETs consist of a heterostructure with ferroelectrics and polar semiconductors. Their spontaneous polarizations can be expected to interact with each other and to generate the two-type of interfaces, namely the depletion state with small depolarization field and the high carrier accumulated state, as mentioned in the subsection 1.2.2. To minimize the mismatch of the charge density at the interface, the amounts of the spontaneous polarizations of the ferroelectrics and the polar semiconductors should be close. Therefore, ZnO and YbMnO₃ were utilized as a polar semiconductor and a ferroelectric, respectively.

ZnO is a remarkable material due to its notable characteristics, such as the wide and direct band gap, the strong exciton binding energy, the wide transparency and the pyroelectric nature. Because of these properties, ZnO has been investigated as the ultraviolet lay sources, the light emitting diodes in the blue region of the spectrum, the transparent thin film transistors and the wide variety of sensors [1–5]. ZnO has the largest spontaneous polarization among oxide semiconductors ($5 \mu\text{C}/\text{cm}^2$) [6, 7]. YbMnO₃ is known to be a multiferroic (ferroelectric and ferromagnetic) material with a hexagonal crystal structure. The spontaneous polarization of YbMnO₃ is almost equal to that of ZnO [8, 9].

Fukushima et al. reported the operation properties of CP-type FeFETs. However, the detail conduction mechanisms and the influences of polarizations to the electronic transport have not been revealed. Thus, in this chapter, the electronic transport properties

of a YbMnO₃/ZnO heterostructure were investigated to discuss the contribution of the polarization of the ferroelectric to the conduction. The carriers transporting in semiconductors are scattered by various mechanisms, such as polar optical phonon scattering, acoustic phonon scattering and ionized impurity scattering. The carrier transport was reported to be strongly affected by the electrostatic potential of trapped charge on the grain boundaries, even epitaxial films [10]. For this reason, the influence of grain boundary scattering is taken into account.

2.2 Preparation and structural characterization of YbMnO₃/ZnO heterostructures

ZnO thin films with a thickness of 20 nm were prepared on (111) yttrium-stabilized zirconia (YSZ) substrates by using a PLD method (Fig. 2.1) at a substrate temperature of 500°C and an oxygen pressure of 2.3×10^{-5} Torr. ZnO thin films were annealed at 1000°C for 1 h because it is reported that ZnO films with an atomically flat surface can be obtained by high temperature annealing [11]. After the annealing, the electrodes were deposited on the films and patterned into a Hall bar shape by using a photolithography method. The YbMnO₃ films with a thickness of 60 nm were deposited on these structures by using the PLD method at 714°C and 5.0×10^{-2} Torr. The sample structures were shown in Fig.2.2. The surface morphology of the samples was observed by using atomic force microscopy (AFM: Nanoscope III, Veeco Instruments, NY). The crystallographic structure was analyzed by using X-ray diffraction (XRD: X'Pert-MRD, Philips, Amsterdam, The Netherlands). The electrical properties were characterized by using the resistivity and the Hall-effect measurements in the temperature region from 80 to 300 K at a magnetic field of 0.76 T.

Figure 2.3 shows the surface morphologies of the as-grown and the annealed ZnO thin films. The as-grown film has small grains and pits. The grains become large and the

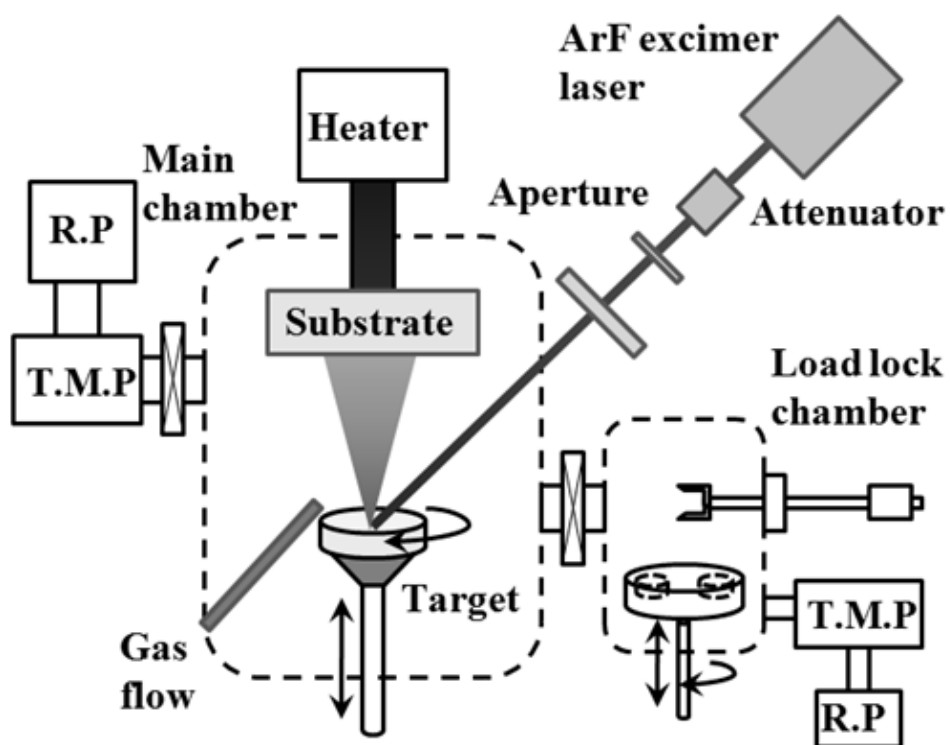


Fig. 2.1 Schematic illustration of the PLD systems

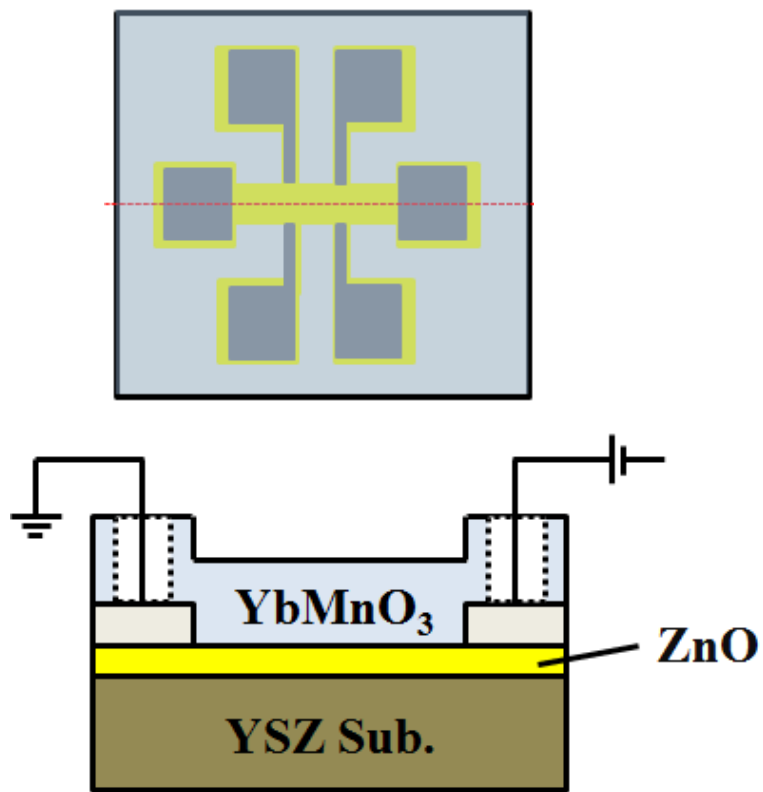


Fig. 2.2 (a) The top and (b) the cross-sectional view of sample structures

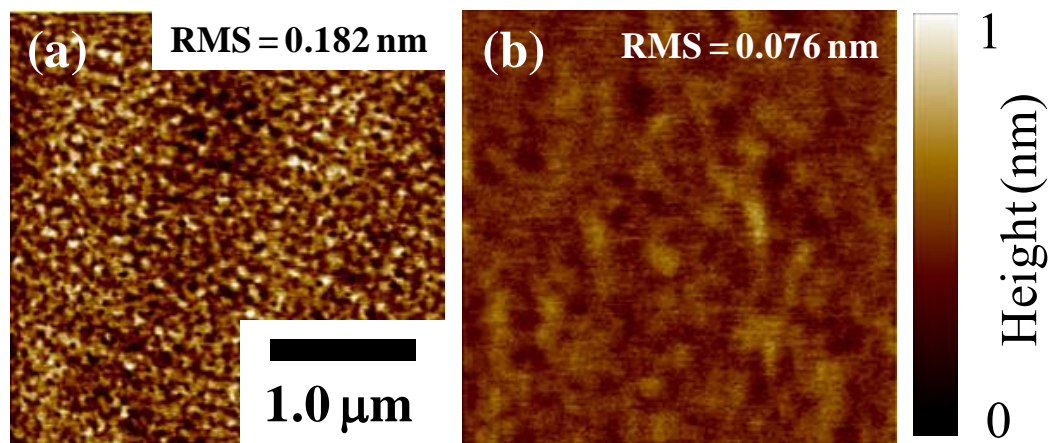


Fig. 2.3 The surface morphology of the ZnO thin films: (a) as-grown and (b) annealed at 1000°C.

root mean square (RMS) for the surface roughness becomes lower by annealing at 1000°C. From the Hall-effect measurement, the carrier concentration was found to be decreased from 10^{20} cm^{-3} to 10^{18} cm^{-3} by the annealing treatment, which indicates that the defects in the ZnO thin films are reduced by an atomic migration and a flocculation of the grains owing to the annealing treatment.

The XRD profiles of the annealed ZnO thin film and the YbMnO₃/ZnO heterostructure are shown in Fig. 2.4. The results indicate that the YbMnO₃ film on the ZnO film has a <0001> orientation, which is along the direction of the spontaneous polarization of YbMnO₃. The broadness of the YbMnO₃ 0004 peak in the 2 θ - ω scan should be caused by the distributed lattice mismatches because the YbMnO₃ films were deposited on substrates with Hall bar structures in which YbMnO₃ films had different lattice strains depending on the location. The rocking curve of the YbMnO₃ 0004 peak has a small value of the full width at half maximum (0.058°). Therefore, the YbMnO₃ film is strongly oriented in the c-axis direction. The shift of the ZnO 0002 peak after the deposition of YbMnO₃ indicates the shrinkage of the c-lattice constant. The origin of the shrinkage will be discussed later in next section.

2.3 Electronic transport properties of YbMnO₃/ZnO heterostructures

Figure 2.5 shows the temperature dependences of the conduction properties of the annealed ZnO thin film and the YbMnO₃/ZnO heterostructure. The carrier concentration of the ZnO thin film is almost constant near room temperature and gradually decreases at temperatures below 200 K. The mobility of the ZnO thin film decreases with decreasing temperature. Compared with the ZnO thin film, the YbMnO₃/ZnO heterostructure has a lower carrier concentration and mobility over the whole temperature range. From the temperature dependence of the conductivity (Fig. 2.5(c)), the activation energies of

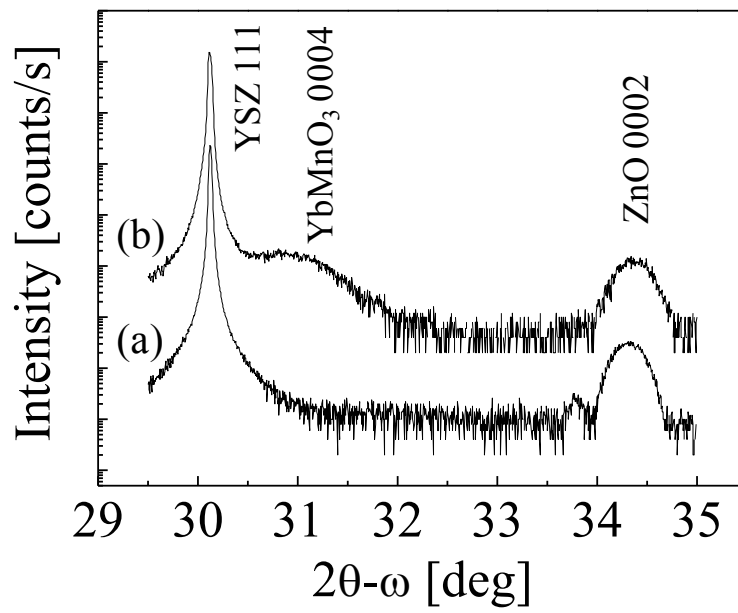


Fig. 2.4 The XRD profiles of the ZnO thin film (a) and the YbMnO₃/ZnO heterostructure (b) in the ω -angle range from 29.5° to 35°.

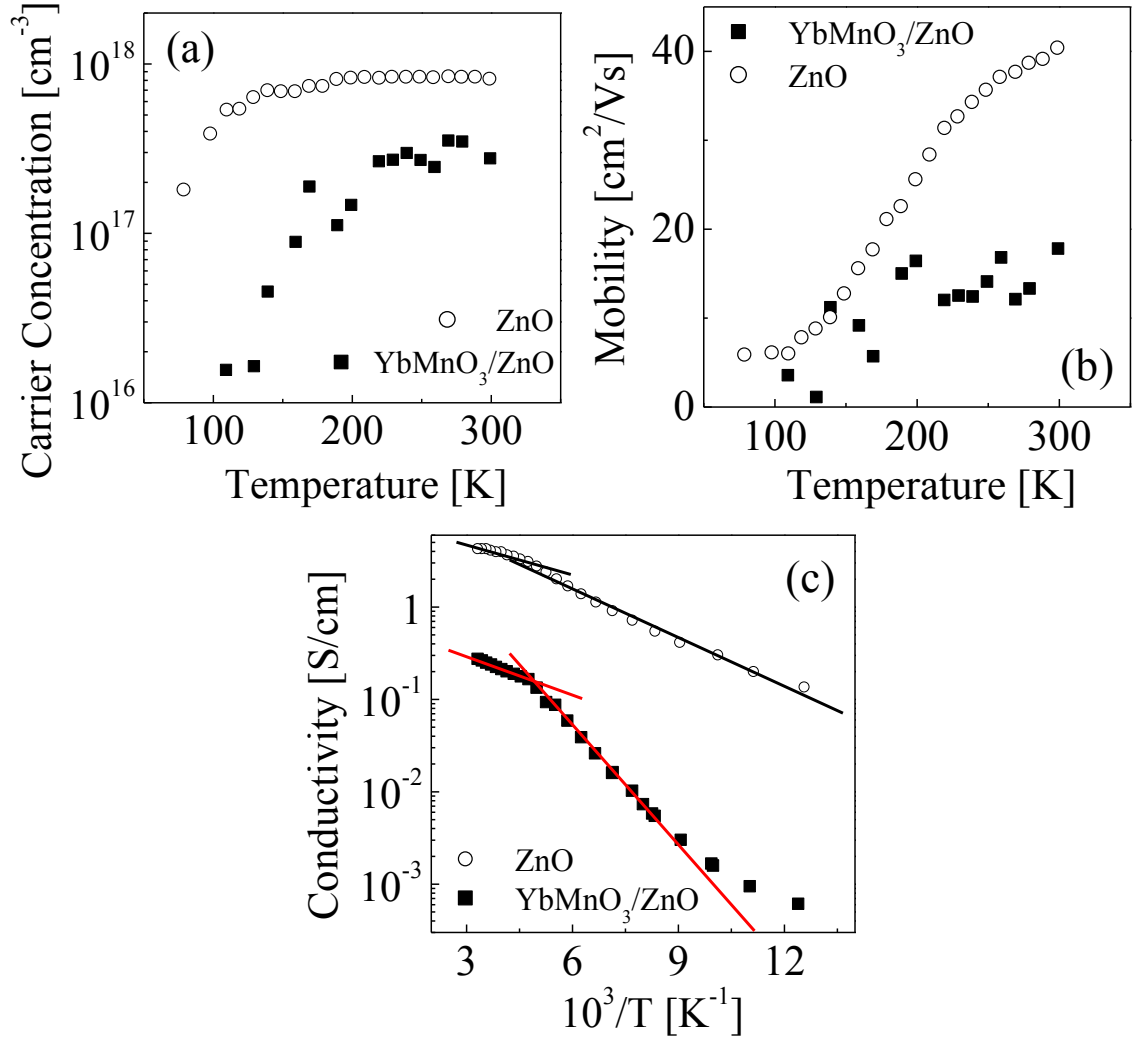


Fig. 2.5 The electrical properties of the ZnO thin film (open circles) and YbMnO₃/ZnO heterostructure (filled squares) in the temperature range from 80 K to 300 K. The carrier concentration (a), the mobility (b) and the conductivity (c) are shown.

conductivity for the ZnO thin film and the YbMnO₃/ZnO heterostructure were obtained as 9.48 and 13.8 meV near room temperature and as 14.7 and 36.2 meV at temperatures lower than 200 K, respectively. Although the activation energy of 36.2 meV is close to that of carrier generation from interstitial zinc ions [12], it was impossible to determine the origin of the other activation energies of 9.48 meV, 13.8 meV and 14.7 meV. To investigate the conduction properties in detail, the temperature dependence of the mobility is analyzed by using the various scattering mechanisms, including (a) the polar optical phonon scattering, (b) the acoustic phonon scattering through the deformation potential and (c) the piezoelectric potential, (d) the ionized impurity scattering and (e) the grain boundary scattering. Table 1 gives the material parameters used for the analysis of the ZnO films. In this analysis, it is assumed that only a single donor with an energy level of 30 meV existed in the ZnO thin films. The scattering factors were determined by using the following parameters and equations:

(a) The corresponding mobility (μ_{pop}) is given by

$$\mu_{pop} = \frac{3\pi\hbar\epsilon_0}{2em^*n(\omega_{LO})} \sqrt{\frac{2\pi\hbar}{\omega_{LO}}} \frac{1}{(\epsilon_\infty^{-1} - \epsilon_0^{-1})} \frac{1}{(T_D/T)^{3/2} e^{T_D/2T} K_1(T_D/2T)}, \quad (2.1)$$

where ϵ_0 and ϵ_∞ are the relative low- and high-frequency dielectric constants, T_D is the Debye temperature and $K_1(t)$ is the Bessel function of the first kind.

(b) The acoustic-mode lattice vibrations induce a deformation potential D_{ac} . The corresponding mobility (μ_{ac}) can be written as

$$\mu_{ac} = \frac{2\sqrt{2\pi}e\hbar^4\rho v_s^2}{3m^{*5/2}(k_B T)^{3/2} D_{ac}^2}. \quad (2.2)$$

(c) The piezoelectric coupling coefficient P_\perp is taken from Ref. 13. Since the current flows perpendicular to the c-axis, a piezoelectric coupling coefficient of 0.21 was used. The corresponding mobility (μ_{pz}) is given by

Table 1. Material parameters of ZnO.

Parameter	Symbol (unit)	Value
Electron effective mass	m^*	$0.31 m_0$
High-frequency dielectric constant	ϵ_0	3.72
Static dielectric constant	ϵ_∞	8.12
Polar phonon Debye temperature	T_D (K)	837
Mass density	ρ (g/cm ³)	5.67
Piezoelectric coupling constant	P_\perp	0.21
Acoustic-mode deformation potential	D_{ac} (eV)	15
Valence of ion	Z	2
Donor level	E_D (meV)	30

$$\mu_{pz} = \frac{16\sqrt{2\pi}e\epsilon\hbar^2\rho v_s^2}{3(eP_{\perp})^2 m^{*3/2}} (k_B T)^{-1/2}. \quad (2.3)$$

(d) The mobility affected by the ionized impurity scattering (μ_{ii}) is given by

$$\mu_{ii} = \frac{64\sqrt{\pi}\epsilon^2}{n_i Z^2 e^3 m^{*1/2}} (2k_B T)^{\frac{3}{2}} \left[\log(1 + \xi_0) - \frac{\xi_0}{1 + \xi_0} \right], \quad (2.4)$$

where m^* is the effective mass, Z is the valence of the ion, n_i is the ionized impurity concentration and ξ_0 is a variable number defined by the equation

$$\xi_0 = \frac{24\epsilon m^* (k_B T)^2}{\hbar^2 e^2 n}. \quad (2.5)$$

(e) The mobility affected by the grain boundary (μ_{gb}) is given by [14, 15]

$$\mu_{gb} = qL \left(\frac{1}{2\pi m^* k_B T} \right)^{\frac{1}{2}} \exp\left(-\frac{qV_b}{k_B T} \right), \quad (2.6)$$

where L is the grain size and qV_b is the potential barrier height on the grain boundary.

When the Fermi level is higher than all the trap levels, V_b is given by

$$V_b = \frac{Q_i^2}{8\epsilon_s n}, \quad (2.7)$$

where Q_i is the trapping state density of the grain boundary. It is obvious that, from Eqs. (2.6) and (2.7), carrier scattering by the grain boundary depends on two parameters, L and Q_i . Therefore, the carrier scattering on the grain boundary is analyzed by fitting with appropriate values of L and Q_i .

Figure 2.6 shows the result of the fitting analysis with Eqs. (2.1)-(2.7) for the temperature dependence of the mobility of the ZnO thin film and the YbMnO₃/ZnO heterostructure. The estimated the grain size of the ZnO film is 10 nm from the result of the fitting analysis. Since the thickness of the ZnO thin films is only 20 nm, a grain size of 10 nm should be reasonable. It is also assumed that the trapping state density of the grain

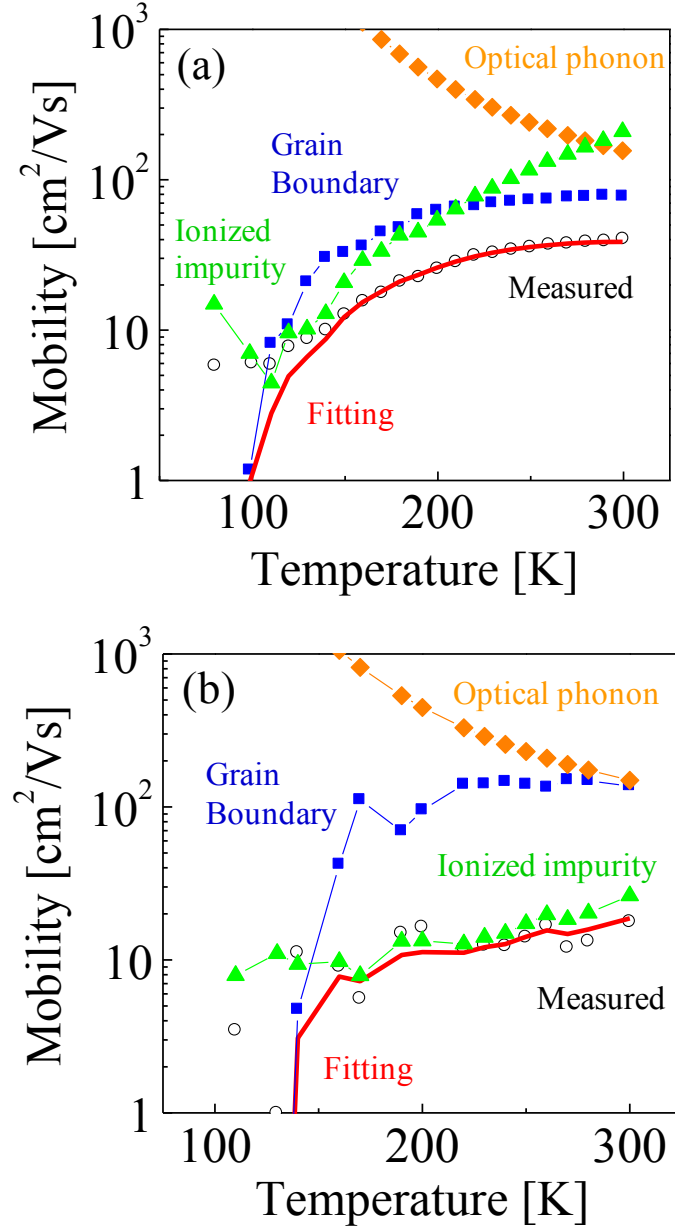


Fig. 2.6 Components of the mobility of the ZnO thin film (a) and the YbMnO₃/ZnO heterostructure (b) fitted by various scattering factors. The fitting curves are shown by solid lines and experimental data are shown by open circles.

boundary was constant over whole temperature range. The fitting analysis revealed that the ionized impurity concentration and the trapping state density of the grain boundary in the ZnO thin film were $3.2 \times 10^{17} \text{ cm}^{-3}$ and $8.1 \times 10^{11} \text{ cm}^{-2}$, respectively. The predominant scattering mechanism in the ZnO thin film is grain boundary scattering at the temperatures near room temperature and gradually turns ionized impurity scattering with decreasing temperature. The barrier height of the grain boundary in the ZnO thin film is probably almost constant over the whole temperature range because there is little change with the carrier concentration. This indicates that the influence of the ionized impurity scattering becomes larger than that of the grain boundary scattering at lower temperatures. Meanwhile, the ionized impurity concentration and the trapping state density of the grain boundary in the YbMnO₃/ZnO heterostructure are estimated as $4.0 \times 10^{19} \text{ cm}^{-3}$ and $2.8 \times 10^{11} \text{ cm}^{-2}$, respectively. Compared with the ZnO thin film, the ionized impurity concentration increases two orders in magnitude and the trapping state density decreases by less than half. Therefore, it is suggested that the dominant scattering mechanism in the YbMnO₃/ZnO heterostructure is the ionized impurity scattering.

Here, the possible origins of the changes in the carrier transport properties will be discussed. One possible origin is thermal diffusion of Mn into the ZnO layer because of the YbMnO₃ film was deposited at a substrate temperature of 714°C. The conductivity of ZnO:Mn is reported to decrease to several orders of magnitude less than that of the undoped ZnO film [16, 17], which corresponds to the presented results. However, it has also reported that the c-lattice constant of ZnO increases in proportion to the Mn concentration because of substituting Mn²⁺ with an ionic radius of 0.66 Å for Zn²⁺ with an ionic radius of 0.60 Å, [18], which does not correspond with the shrinkage of c-lattice constant of the ZnO thin film shown in Fig. 2.4. Therefore, it is suggested that a small amount of Mn diffuses thermally into the ZnO thin film during the deposition of YbMnO₃.

It is deduced that the origin of the shrinkage of the c-lattice constant is a relaxation of the lattice strain from the YSZ substrate. Another possible origin of the changes in the carrier transport properties is a contribution of the spontaneous polarizations of YbMnO_3 . It is reasonable that the spontaneous polarization of YbMnO_3 directs upward and downward equally for the as-grown state. In a microscopic region, a positive or a negative polarization domain of YbMnO_3 would have an influence on the conduction by generating disorder potential at the interface between YbMnO_3 and ZnO or by depleting the ZnO layer partly. Therefore, it is suggested that this microscopic effect of the spontaneous polarization causes the decreases in the carrier concentration and in the mobility and causes ionized impurity scattering.

2.4 Conclusions

The conduction property of $\text{YbMnO}_3/\text{ZnO}$ heterostructure, which is the fundamental structure of CP-type FeFETs, was investigated to discuss the effect of the spontaneous polarization of YbMnO_3 on the electronic transport of the ZnO layer. The carrier concentration and the mobility of the ZnO layer were shown to be decreased by the deposition of YbMnO_3 . As a result of an analysis using the various carrier scattering factors, the dominant scattering mechanism of the $\text{YbMnO}_3/\text{ZnO}$ heterostructure is the ionized impurity scattering while the conduction property of the ZnO thin film is dominated by grain boundary scattering. The change in the dominant factor of conduction is explained by the effect of the spontaneous polarization of YbMnO_3 . The domain of the spontaneous polarization of YbMnO_3 generates a partially depleted region in the ZnO layer and the disorder potential and has an influence on the conduction of the $\text{YbMnO}_3/\text{ZnO}$ heterostructure.

References

- [1] Z. K. Tang, G. K. L. Wong, P. Yu, M. Kawasaki, A. Ohtomo, H. Koinuma, and Y. Segawa, Appl. Phys. Lett. **72**, 25 (1998).
- [2] M. H. Huang, S. Mao, H. Yan, Y. Wu, H. Kind, E. Weber, R. Russo, and P. Yang, Science **292**, 1897 (2001).
- [3] A. Tsukazaki, M. Kubota, A. Ohtomo, T. Onuma, K. Ohtani, H. Ohno, S. F. Chichibu, and M. Kawasaki, Jpn. J. Appl. Phys. **44**, 21 (2005).
- [4] A. Hongsingthong, T. Krajangsang, I. A. Yunaz, S. Miyajima, and M. Konagai, Appl. Phys. Express **3**, 051102 (2010).
- [5] N. Koshizaki and T. Oyama, Sensors and Actuators B **66**, 119 (2000).
- [6] A. D. Corso, M. Posternak, R. Resta, and A. Baldereschi, Phys. Rev. B **50**, 15 (1994).
- [7] J. Jerphagnon and H. W. Newkirk, Appl. Phys. Lett. **18**, 6 (1971).
- [8] K. H. Hellwege and A. M. Hellwege, *Landolt-Bornstein* (Springer-Verlag, Berlin Heidelberg New York, 1981) Vol. **16**, p.164.
- [9] G. A. Smolenskii and V. A. Bokov, J. Appl. Phys. **35**, 3 (1964).
- [10] W. R. Liu, W. F. Hsieh, C. H. Hsu, K. S. Liang and F. S. S. Chien, J. Cryst. Growth **297**, 294 (2006).
- [11] T. Kamiya, Y. Takeda, K. Nomura, H. Ohta, H. Yanagi, M. Hirano, and H. Hosono, Crystal Growth & Design **6**, 11 (2006).
- [12] D. C. Look and J. W. Hemsky, Phys. Rev. Lett. **82**, 12 (1999).
- [13] D. C. Look, D. C. Reynolds, J. R. Sizelove, C. W. Litton, G. Cantwell, and W. C. Harsch, Solid State Commun. **105**, 399 (1998).
- [14] F. M. Hossain, J. Nishii, S. Takagi, A. Ohtomo, T. Fukumura, H. Fujioka, H. Ohno, H. Koinuma, and M. Kawasaki, J. Appl. Phys. **94**, 12 (2003).
- [15] J. Y. W. Seto, J. Appl. Phys. **46**, 5247 (1975).

- [16] T. Oshio, K. Masuko, A. Ashida, T. Yoshimura, and N. Fujimura, J. Appl. Phys. **103**, 093717 (2008).
- [17] Z. Zhou, K. Kato, T. Komaki, M. Yoshino, H. Yukawa, M. Morinaga, and K. Morita, J. Euro. Ceram. Soc. **24**, 139 (2004).
- [18] K. Masuko, A. Ashida, T. Yoshimura, and N. Fujimura, J. Appl. Phys. **103**, 043714 (2008).

Chapter 3: Effect of Ferroelectric Polarization on Electronic Transport Properties in Ferroelectric/Polar Semiconductor Heterostructures

3.1 Introduction

In the case of conventional FETs with a paraelectric gate, the gate gives uniform potential to the semiconductor channel. On the other hand, the ferroelectric gate forms a steep potential change caused by the ferroelectric domain boundary that can be changed by applying the electric fields. No reports discuss such an effect, even though it should be important in improving the performance of the FeFETs. In this chapter, therefore, the effect of the ferroelectric polarizations and their domain structure on the electronic transport in the semiconductor channel is focused.

In chapter 2, the YbMnO_3 films were utilized as ferroelectric layer and the dominant scattering mechanism in the ZnO thin films was revealed to change from the grain boundary scattering to the ionized impurity scattering by the deposition of the ferroelectric YbMnO_3 , which suggests that ferroelectric polarization may have an influences to the electron transport in the ZnO thin films. However, there is another possibility that the change in the scattering mechanism might be caused by the thermal diffusion of Yb or Mn into the ZnO, because the deposition temperature of the YbMnO_3 was 714°C , which is higher than that of ZnO (500°C). To avoid the influences of thermal diffusion, the low temperature process of the ferroelectrics is required. Therefore, the organic ferroelectric of P(VDF-TeFE) is utilized due to the low crystallization temperature ($\sim 150^\circ\text{C}$) without any special preparation process [1, 2]. P(VDF-TeFE) is widely known as organic ferroelectrics which is construct with the chain structures of CH_2 and CF_2 . When

the voltage is applied across the P(VDF-TeFE) layer, their polarization can be reversed through the rotation of the molecular chain [3]. Moreover, P(VDF-TeFE) has a comparable remanent polarization ($5.2 \mu\text{C}/\text{cm}^2$) to the spontaneous polarization of ZnO [4].

The CP-type FeFETs constructed of P(VDF-TeFE)/ZnO Hall bar structure with a gate stack were fabricated and characterized. The Hall-effect measurements after various poling voltages applied to P(VDF-TeFE) were performed to discuss the effect of the ferroelectric domain structure on the electronic transport property in the CP-type FeFETs.

3.2 Experimental procedures

The ZnO thin films with a thickness of 20 nm were deposited on (111) YSZ substrates by a PLD method at the substrate temperature of 500°C and the oxygen pressure of 1.4×10^{-5} Torr. To relax the lattice misfit strain in the ZnO thin films caused by large lattice mismatch (10%) between ZnO and YSZ, annealing treatment at 1000°C was carried out in air. After the annealing, holes were formed in ZnO thin films by the Ar ion milling and the source and drain electrodes of Au/Ti were deposited on the holes in the ZnO films to obtain a ZnO Hall bar structures with a flat surface. Then the ZnO thin films were processed into a Hall bar shape by photolithography. P(VDF-TeFE) with a molar content ratio (VDF/TeFE) of 80/20 was dissolved in methylethylketone by adjusting the solution concentration to 7 wt.%. The solution was spin-coated to the ZnO Hall bar structure. The thickness of the obtained P(VDF-TeFE) layer was approximately 400 nm. To crystallize the P(VDF-TeFE) films, the samples were annealed in air at 145°C for 30 min. The gate electrodes of Au were deposited on P(VDF-TeFE)/ZnO/YSZ by electron beam evaporation and patterned by photolithography. Figure 3.1(a) shows the schematic of the cross section of the P(VDF-TeFE)/ZnO/YSZ structures. The channel length (L) and width (W) of the Hall bar structures are 700 and 100 μm , respectively. The length between the voltage

measurement terminals for resistivity measurement is 120 μm . The shape of the Hall bar structure is shown in Fig. 3.1(b). The dielectric and electric properties of the FeFETs with the P(VDF-TeFE)/ZnO/YSZ hetero-structure were measured by an LCR meter (HP4284A, Hewlett Packard, Palo Alto, CA) and a picoammeter (HP4140B, Hewlett Packard). The poling voltage dependence of the electronic transport properties was evaluated using a Hall effect measurement system (ResiTest 8300, Toyo Technica, Tokyo, Japan). To characterize the dielectric properties of the P(VDF-TeFE) films, the Au/P(VDF-TeFE)/Au/Ti capacitors were also fabricated in the same samples.

3.3 Results and discussion

3.3.1 Effect of ferroelectric domain structures in electronic transport properties of poly(vinylidene fluoride-tetrafluoroethylene)/ZnO heterostructures

The relative permittivity-voltage (ϵ_r - V) characteristic of the P(VDF-TeFE) capacitors is shown in Fig. 3.2(a). A typical butterfly-shaped change of ϵ_r originating from the ferroelectric polarization switching of the P(VDF-TeFE) films is observed. The relative permittivity of the P(VDF-TeFE) films at 40 V is calculated to be 5.2. Figure 2.2(b) shows the P - V characteristics of the P(VDF-TeFE) capacitors. The saturated polarization, the remanent polarization and the coercive voltage of the P(VDF-TeFE) films are confirmed to be 3.4 and 3.0 $\mu\text{C}\cdot\text{cm}^{-2}$, and 44 V, respectively. By using the obtained remanent polarization, it is calculated that the carrier concentration in the ZnO thin films induced or depleted by the polarization of P(VDF-TeFE) is $9.4 \times 10^{18} \text{ cm}^{-3}$.

The drain current-gate voltage (I_D - V_G) characteristics of the P(VDF-TeFE)/ZnO structure are shown in Fig. 3.3. The measurements were carried out at the fixed drain

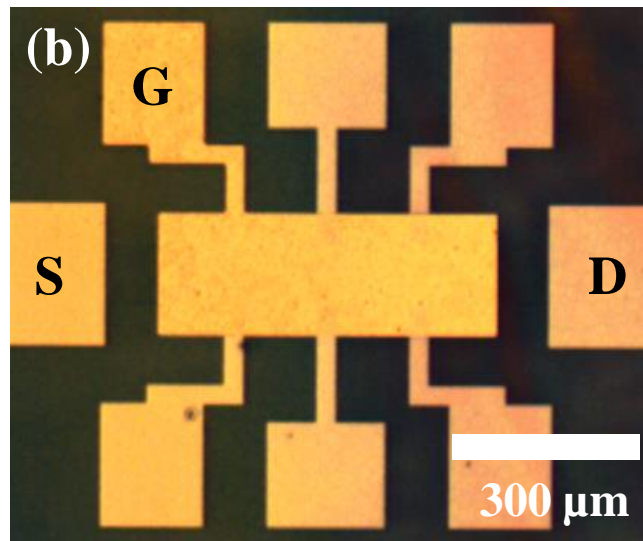
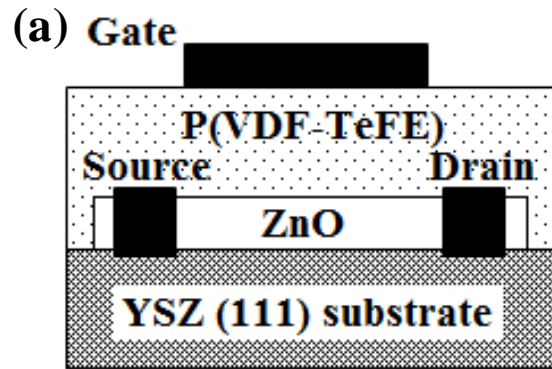


Fig. 3.1 Schematic illustration (cross-sectional-view) (a) and micrograph (top-view) (b) of the P(VDF-TeFE)/ZnO/YSZ Hall bar structure.

voltage (V_D) of 0.1 V by applying a sweeping gate voltage (V_G) in the range from -100 to 100 V. The I_D - V_G curve shows the counterclockwise hysteresis loop corresponding to the ferroelectric polarization switching of P(VDF-TeFE). From the I_D - V_G curve, the field-effect mobility (μ_{FE}) of the P(VDF-TeFE)/ZnO structure were calculated using [5]

$$I_D = \mu_{FE} Q_i V_D \frac{W}{L}, \quad (3.1)$$

where Q_i is the induced charges at the interface between the ferroelectrics and the semiconductors, L is the channel length, and W is the channel width. The induced charge at the interface consists of two components: the ferroelectric polarization and the electrostatic charge induced by the gate bias voltage. Thus Q_i is given by

$$Q_i = P + C_f V_G, \quad (3.2)$$

where P and C_f are the ferroelectric polarization and the dielectric component of the capacitance of the ferroelectrics, respectively. From eqs. (3.1) and (3.2), the field-effect mobility is calculated as

$$\mu_{FE} = \frac{\frac{\partial I_D}{\partial V_G} \frac{\partial V_G}{\partial Q_i} \frac{L}{W}}{V_D}. \quad (3.3)$$

$\partial I_D / \partial V_G$ and $\partial V_G / \partial Q_i$ are estimated to be $6.1 \times 10^{-9} \text{ A} \cdot \text{V}^{-1}$ and $6.0 \times 10^7 \text{ V} \cdot \text{cm}^2 \cdot \text{C}^{-1}$ from the I_D - V_G (Fig.3.3) and P - V (Fig. 3.2(b)) characteristics at the saturated region, respectively. Using these values, the field-effect mobility of the P(VDF-TeFE)/ZnO structure is calculated as $26 \text{ cm}^2 \cdot \text{V}^{-1} \cdot \text{s}^{-1}$.

To investigate the effect of the ferroelectric domain on the electronic transport property of the ZnO thin films in detail, the resistivity and the Hall-effect measurements were carried out after various poling treatments at gate voltages from -100 to 100 V changed in 20 V steps. Note that these measurements were performed under the open gate

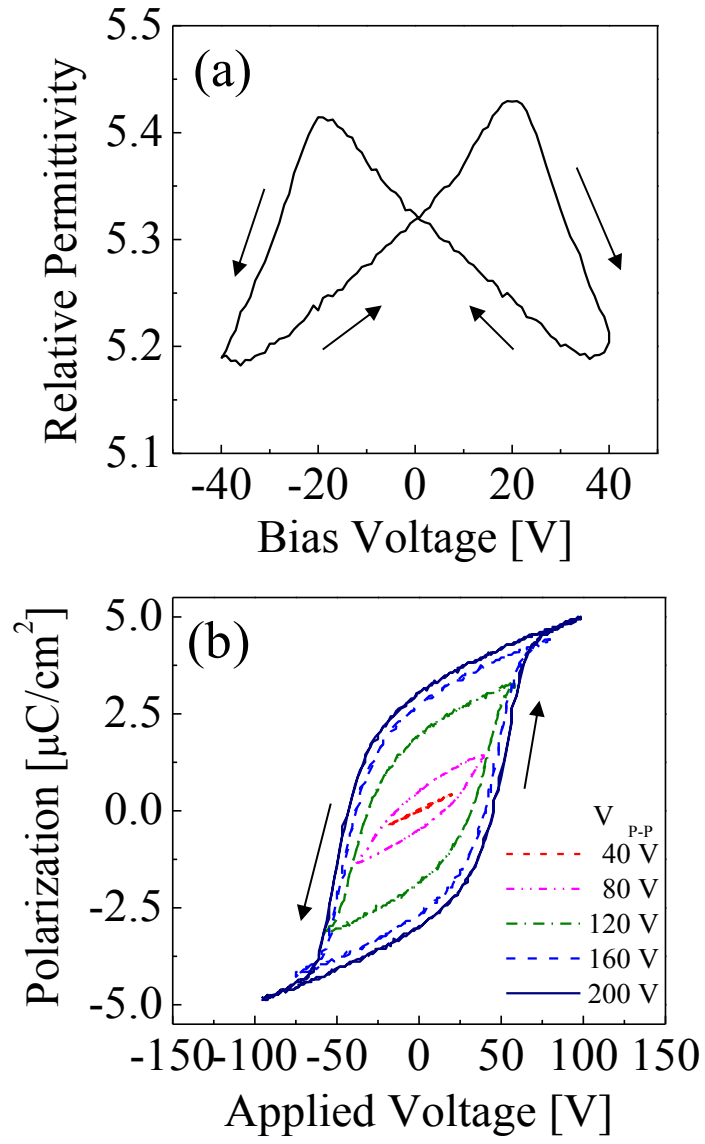


Fig. 3.2 The ϵ_r - V characteristic (a) and the P - V characteristics (b) of the P(VDF-TeFE) capacitor.

circuit (zero bias) condition after the poling treatments. Figure 3.4(a) shows the change in the conductivity of the P(VDF-TeFE)/ZnO structure as a function of the poling voltage. The conductivity exhibits a counterclockwise hysteresis loop and is comparable to the conductivity calculated from the I_D - V_G characteristics shown in Fig. 3.3. The change in the carrier concentration corresponding to Fig. 3.4(a) is shown in Fig. 3.4(b). The carrier concentration also shows the hysteresis behavior originating from the ferroelectric polarization switching of P(VDF-TeFE). The carrier concentration can be divided into lower and higher regions. The higher carrier concentration region apparently indicates the accumulation state and the lower region corresponds to the channel region, which includes the depletion region. The carrier concentration of the ZnO thin films before the deposition of P(VDF-TeFE) is $1.3 \times 10^{18} \text{ cm}^{-3}$. The accumulated electrons at the interface between P(VDF-TeFE) and ZnO owing to the spontaneous polarization of the ZnO is calculated to be $1.6 \times 10^{19} \text{ cm}^{-3}$. As mentioned above, the carrier concentration induced or depleted by the ferroelectric layer in our sample is $9.4 \times 10^{18} \text{ cm}^{-3}$. Thus the electron concentration of the P(VDF-TeFE)/ZnO structures should be the sum of the electron concentration and is between 7.5×10^{18} and $2.6 \times 10^{19} \text{ cm}^{-3}$. The relatively high carrier concentration even at the negative polarized region shown in Fig. 3.4(b) suggests that the ZnO channel is not completely depleted and the rest of the ZnO channel acts as a conduction path, yielding the high off current in the I_D - V_G characteristics, as shown in Fig. 3.3.

Figure 3.4(c) shows the Hall mobility of the P(VDF-TeFE)/ZnO structure as a function of the poling voltage. Note that the sample was poled before the measurements of the resistivity and the Hall voltage to minimize the effect of depolarization. However in some cases, the polarized states of P(VDF-TeFE) between these measurements might be different. It appears that this is the origin of the relatively high mobility obtained at the

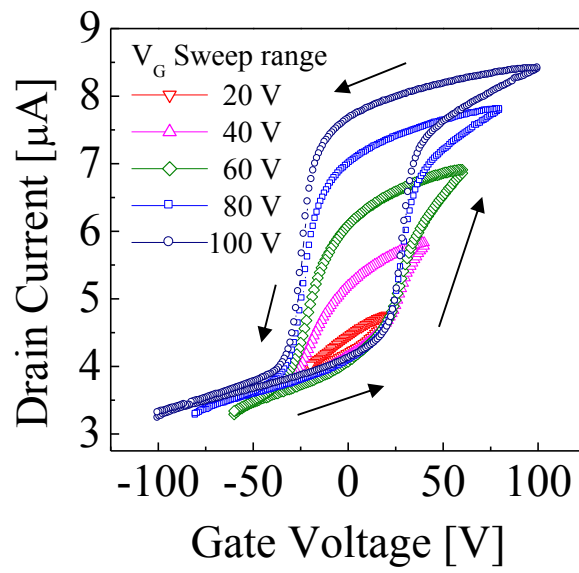


Fig. 3.3 The I_D - V_G characteristics of the P(VDF-TeFE)/ZnO heterostructures.

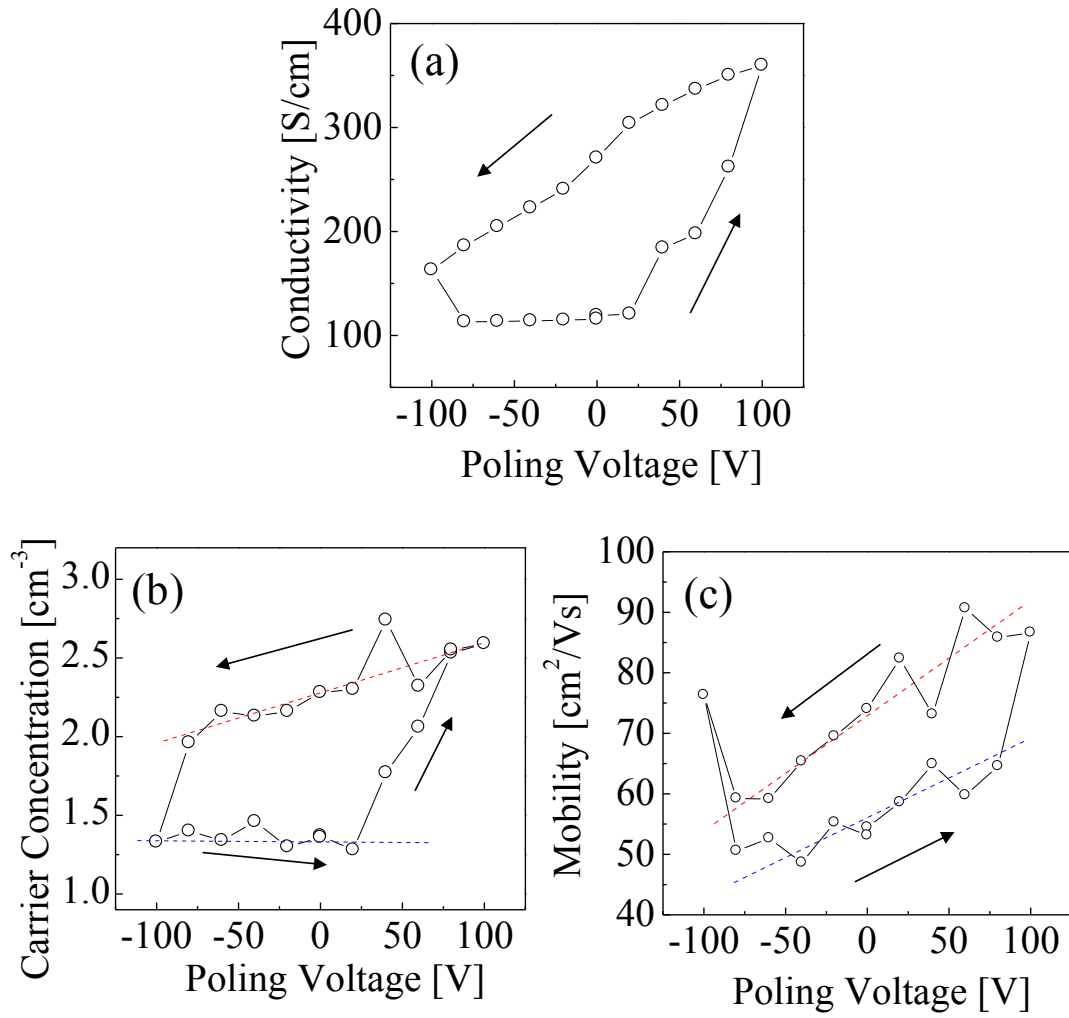


Fig. 3.4 The electronic transport properties of the P(VDF-TeFE)/ZnO structure. The conductivity (a), the carrier concentration (b), and the Hall mobility (c) are shown.

poling voltage of -100 V. When the poling voltage is increased from -80 to 20 V, the Hall mobility shows a gradual increase from 51 to 59 $\text{cm}^2\cdot\text{V}^{-1}\cdot\text{s}^{-1}$. On the other hand, the corresponding carrier concentration shown in Fig. 3.4(b) does not show significant change. It is likely that the results obtained with poling voltage decreased from -80 to 20 V are influenced by the conduction path, which is the region not depleted by the polarization of P(VDF-TeFE), as described above. When the poling voltage decreases from 100 to -80 V, which corresponds to the accumulation state, the Hall mobility gradually decreases from 87 to 59 $\text{cm}^2\cdot\text{V}^{-1}\cdot\text{s}^{-1}$ and the corresponding carrier concentration decreases from 2.5×10^{19} to 2.0×10^{19} cm^{-3} . The Hall mobility is three times higher than the field-effect mobility. The difference between the Hall and field-effect mobilities might be caused by the electron velocity distribution arising from charge trapping [6, 7]. Additionally, in this work, the Hall-effect measurement was carried out without gate bias voltage. Therefore, the disturbance effect generated by the gate voltage is a possible cause of the difference between the Hall and the field-effect mobilities. The decrease in the carrier concentration from 2.5×10^{19} to 2.0×10^{19} cm^{-3} corresponds to a decrease of 1.6 $\mu\text{C}/\text{cm}^2$ in the remanent polarization of P(VDF-TeFE), which is consistent with the P - V characteristics of the P(VDF-TeFE) layer shown in Fig. 3.2(b). Since the decrease in the carrier concentration is not caused by the change in the ionized impurity density, the effect of ionized impurity scattering on the Hall mobility should be little. The grain boundary scattering mechanism is also a possible origin of the decrease in the Hall mobility. However, the decrease in the carrier concentration from 2.5×10^{19} to 2.0×10^{19} cm^{-3} causes the decrease in the Hall mobility of less than 1% . Thus, neither the ionized impurity nor the grain boundary scattering mechanism, which are the dominant scattering mechanisms in typical ZnO thin films, is the dominant scattering mechanism when P(VDF-TeFE) is deposited on top of ZnO. Therefore, the effect of the ferroelectric domain structure as the scattering

mechanism for the P(VDF-TeFE)/ZnO structure is proposed. The Hall mobility at the poling voltage of 100 V is $87 \text{ cm}^2 \cdot \text{V}^{-1} \cdot \text{s}^{-1}$ and it gradually decreases with decreasing poling voltage, whereas the carrier concentration shows only a slight change. In this region, the fully polarized ferroelectric domain after poling at 100 V begins to switch with decreasing poling voltage. Thus the steep potential change corresponding to the ferroelectric domain boundary is generated in the ZnO thin films by the formation of a multidomain structure of the P(VDF-TeFE) films. The electron transport in the ZnO thin films is disturbed through the potential fluctuation in the ZnO thin films corresponding to the ferroelectric domain boundary that is generated by polarization switching. These results indicate that although the electron scattering in the channel is generated by the existence of the domain walls, there might be little effect on the electron scattering originating from ferroelectric polarization if the ferroelectric polarization were fully polarized.

3.3.2 Electrical and electronic transport properties of poly(vinylidene fluoride-tetrafluoroethylene)/ZnO heterostructures with various channel thicknesses

In previous subsection, although the effect of the ferroelectric polarization was investigated, the degeneration layer at ZnO/YSZ interfaces strongly influences in conduction and the operation properties were found to be poor. Therefore, the deposition conditions of the channel layer of ZnO and the sample structures were revised at first. Moreover, the various channel thickness of FeFETs were fabricated to evaluate the electronic transport under ferroelectric gate including the influence of conduction paths distribution along longitudinal direction.

The ZnO thin films were deposited on (111) YSZ at the various substrate temperatures from 500 to 700°C and carried out the Hall-effect measurements. The results are shown in Fig. 3.5. The carrier concentration of ZnO thin films drastically decrease at

the temperature above 620°C and regain at 700°C. The results indicate that the high temperature promotes the formation of high crystal quality films, however, the excess temperature causes the reevaporation of film elements and leads the defect formation.

The ZnO films with a thicknesses from 20 to 500 nm were deposited on (111) YSZ by PLD method at 650°C and 3×10^{-5} Torr. The annealing treatments were performed at 1050°C in air. The surface morphologies of the annealed films which are shown in Fig.3.6 exhibit the flat surfaces with step and terrace structures, although the thinner films show the step bunching structures. The source and drain electrodes of Au/Ti were deposited on the ZnO films by an EB evaporation and the ZnO films were processed into Hall bar shape, which is shown in Fig. 3.7, with a channel width and length of 100 and 320 μm , respectively, by photolithography.

The *P-V* characteristic of a Au/P(VDF-TeFE)/AuTi capacitors which are fabricated in the same sample with the P(VDF-TeFE)/ZnO/YSZ hetero-structures was measured by using a Sawyer-tower circuit. The result is shown in Fig. 3.8. Rectangular hysteresis loop originated from the ferroelectricity of P(VDF-TeFE) is obtained. The remnant and saturated polarizations, and coercive voltage of the P(VDF-TeFE) film are 2.7 $\mu\text{C}/\text{cm}^2$, 3.0 $\mu\text{C}/\text{cm}^2$, and 30 V, respectively.

Figure 3.9(a) shows the capacitance-voltage (*C-V*) characteristics of the P(VDF-TeFE)/ZnO Hall bar structures with various channel thicknesses. The *C-V* characteristics at the channel thicknesses of 500 and 370 nm show the butterfly shape curve originating from the polarization switching of P(VDF-TeFE) and smaller capacitance at negative bias voltage than positive bias voltage which attributed to the depletion of the ZnO channel. The calculated depletion width is 50 and 80 nm for the samples with the channel thicknesses of 500 and 370 nm, respectively. The samples with the channel

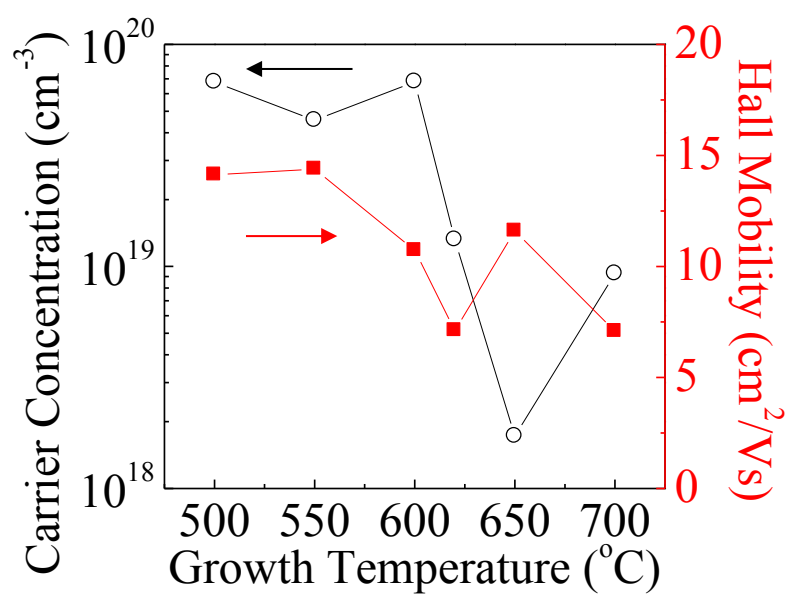


Fig. 3.5 Growth temperature dependence of the carrier concentration (open circles) and Hall mobility (red squares) of the ZnO thin films.

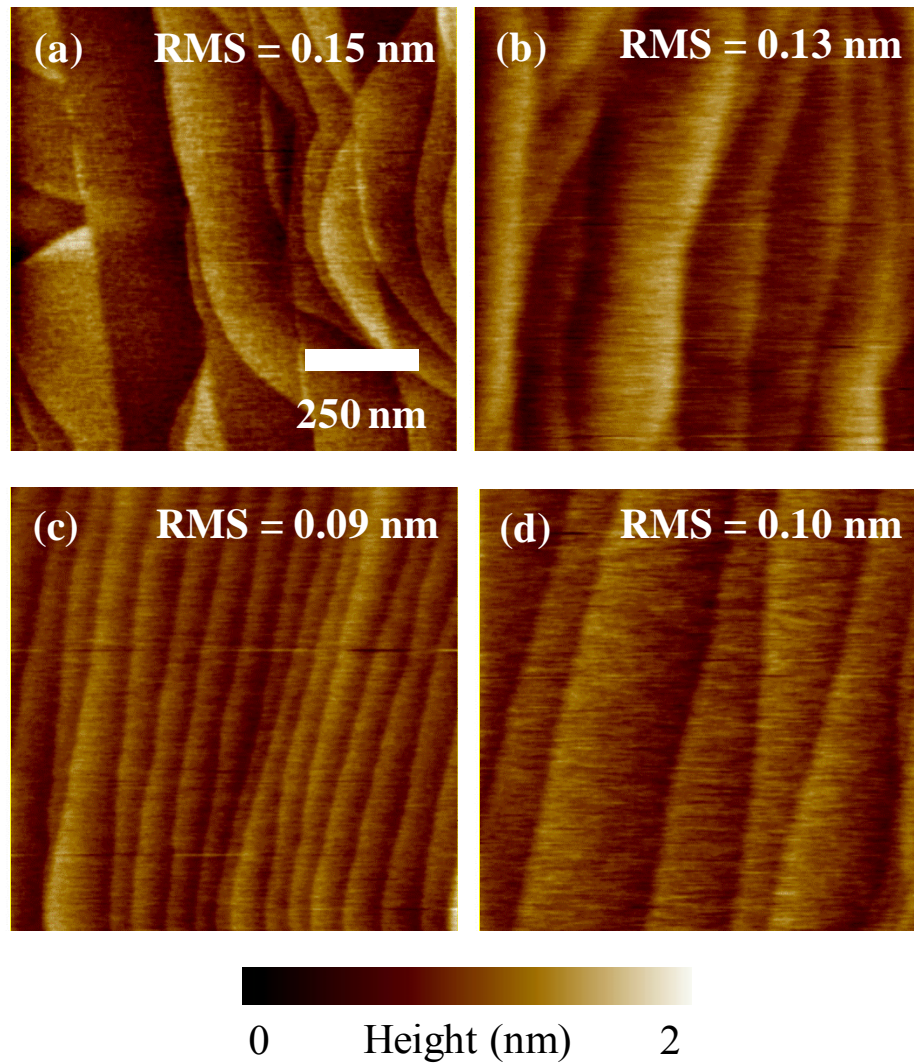


Fig. 3.6 Surface morphology of the annealed ZnO films with the film thicknesses of 20 (a), 100 (b), 370 (c), and 500 nm (d).

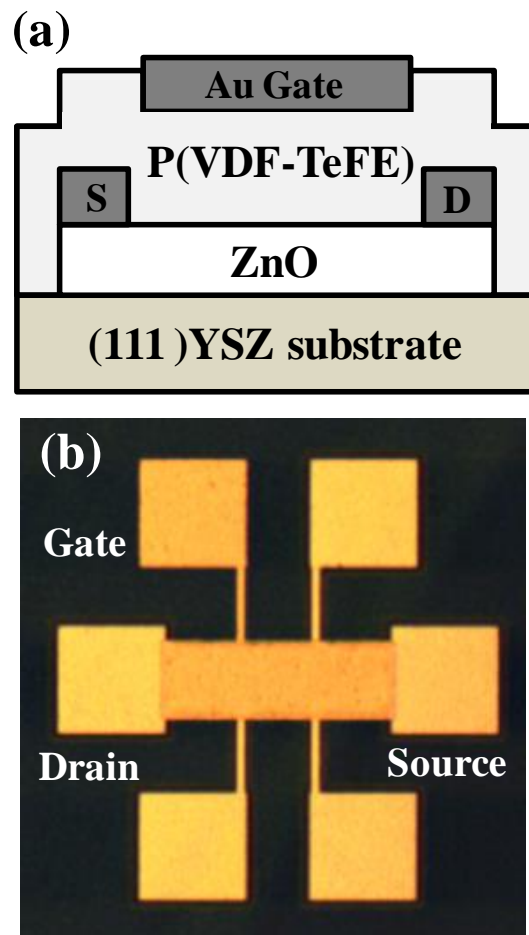


Fig. 3.7 Schematic image of sample structure (a) and micrograph (b) of the P(VDF-TeFE)/ZnO Hall bar structures.

thicknesses of 100 and 20 nm show the typical C - V curves for a MFS structure. The counterclockwise hysteresis loops indicate the ferroelectricity of P(VDF-TeFE) and complete depletion of the ZnO channel. The I_D - V_G characteristics of the P(VDF-TeFE)/ZnO Hall bar structures with various channel thicknesses is shown in Fig. 3.9(b). The I_D - V_G characteristics at the channel thicknesses of 500 and 370 nm show small change in the I_D . On the other hand, at the channel thicknesses of 100 and 20 nm, I_D shows large change by V_G , which is consistent with the complete depletion of the channel as described above. The memory window at a drain current around 2 μ A for the 20 nm thick channel FeFET is found as 57 V which corresponds to the twofold of the coercive voltage of the P(VDF-TeFE) capacitors. This indicates that the counterclockwise hysteresis loop originates from the ferroelectric nature of the P(VDF-TeFE) layer, while the smaller memory window in the 100 nm-channel FeFET also indicates the existence of the trapping state. The ON/OFF ratio of the I_D at a gate voltage of 0 V achieves in an order of 10^5 . The field-effect mobility was calculated from the I_D - V_G curve by using Eq. (3.3). The values of $\partial V_G / \partial Q_i$ and $\partial I_D / \partial V_G$ are estimated from the saturated regions of the P - V and I_D - V_G characteristics, which are shown in Figs. 3.8 and 3.9(b), respectively. The calculated field-effect mobility is shown in Fig. 3.10. The field-effect mobility decreases with decreasing the channel thickness.

To discuss the channel conduction of the FeFETs in detail, the Hall-effect measurements for the ZnO films with and without the P(VDF-TeFE) layer were carried out. Figure 3.11(a) shows the carrier concentrations as a function of the channel thickness. For P(VDF-TeFE)/ZnO, the measurement was carried out at $V_G=0$ V after positive poling treatment, namely the channels set to ON state. Although the carriers in P(VDF-TeFE)/ZnO should be accumulated by the positively polarized ferroelectric layer,

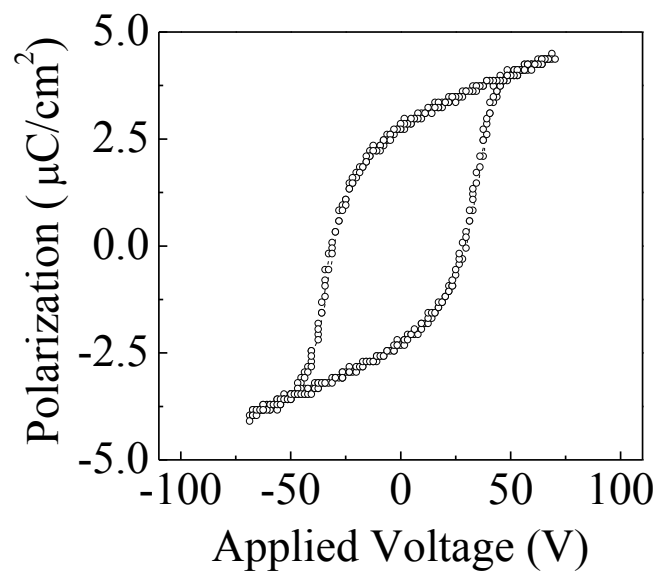


Fig 3.8 The P - V characteristic of an Au/P(VDF-TeFE)/AuTi capacitors measured at 1 kHz.

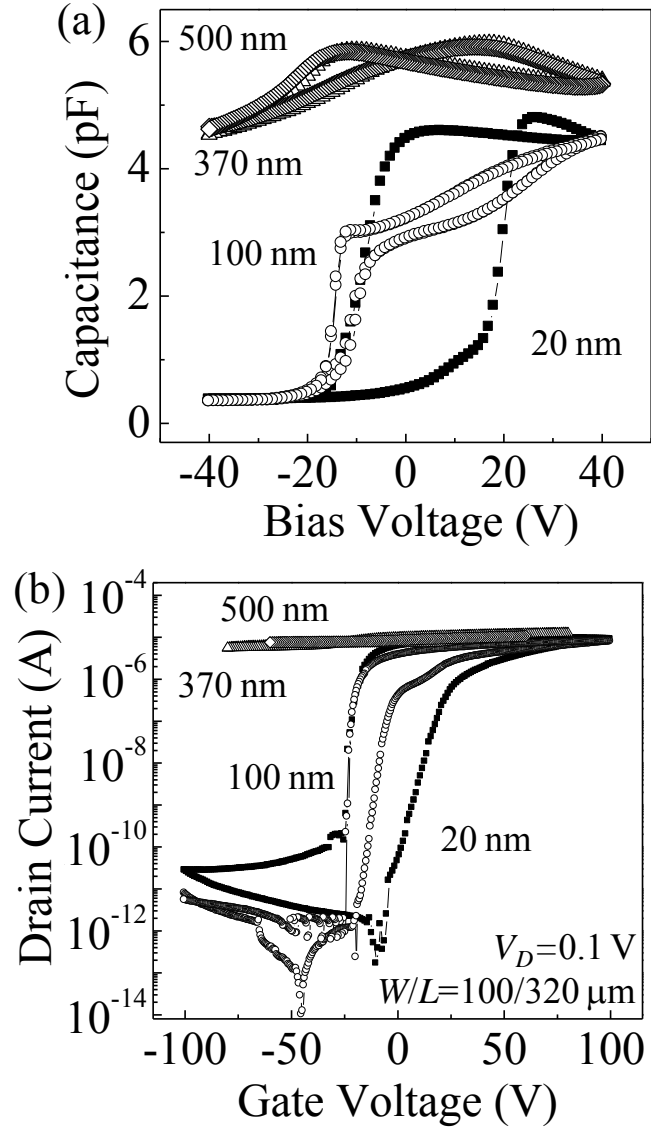


Fig 3.9 The C - V (a) and I_D - V_G (b) characteristics of the P(VDF-TeFE)/ZnO/YSZ hetero-structures with the channel thicknesses from 20 to 500 nm.

the carrier concentration of P(VDF-TeFE)/ZnO is smaller than that of ZnO. One of possible reasons is the existence of the upward polarization domain in the P(VDF-TeFE) layer. When the P(VDF-TeFE) layer is not single domain, it can be expected that the depleted region is formed in the ZnO channel under the upward domain. The reduction of the conductive region causes the lowering of the calculated carrier concentration than the real. Another possible reason is the surface adsorption, because the ZnO films without the P(VDF-TeFE) layer did not receive any passivation treatments. Several reports indicate that the hydrogen adsorption acts as a donor and enlarges the conductivity of ZnO [8–10].

The Hall mobility of the ZnO films with and without the P(VDF-TeFE) layer are shown in Fig. 3.11(b). While the Hall mobility of the ZnO films without the P(VDF-TeFE) layer shows a little increase with increasing the film thickness, it increases largely by the deposition of the P(VDF-TeFE) layer. Therefore, it is suggested that the field effect by the ferroelectric polarization attributes to enlarge the mobility. When the carriers are accumulated by the ferroelectric polarization, the carriers transport near the interface of P(VDF-TeFE)/ZnO. The reduction of the influence of the misfit dislocation at the ZnO/YSZ interface on the carrier transport is possible origin of the enlargement of the Hall mobility. It is known that a degenerate layer exists at the ZnO/YSZ interface even after annealing treatment [11]. In the degenerate layer, the Hall mobility is lower than that in the bulk region owing to the high defect density [12, 13]. Since the conductivity near the interface between P(VDF-TeFE) and ZnO is increased by the carrier induction originating from the ferroelectric polarization, the influence of the degenerate layer is reduced. This higher Hall mobility ensures a good interface with less thermal interdiffusion between P(VDF-TeFE) and ZnO. It is also found that the Hall mobility of P(VDF-TeFE)/ZnO is higher than that of the field-effect mobility shown in Fig. 3.10. The difference between the Hall mobility and the field-effect mobility can be explained by some reasons. One is the

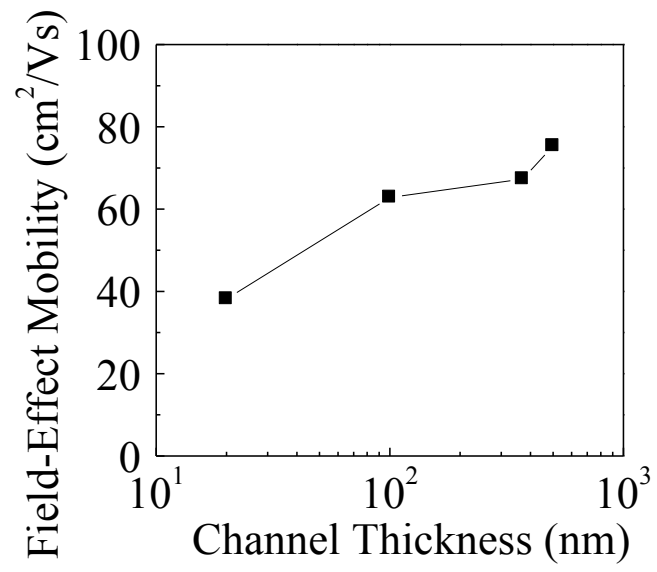


Fig. 3.10 The channel thickness dependence of the field-effect mobility of the P(VDF-TeFE)/ZnO/YSZ hetero-structures.

effect of V_G . While the Hall-effect measurement was carried out at $V_G=0$ V, the field-effect mobility was calculated from the saturation regions of the I_D - V_G curve over $V_G=40$ V. It is known that the field-effect mobility is smaller than the effective mobility due to the influences of the gate voltage [14]. Another reason is the issue of the Hall factor which is the proportional constant of the Hall mobility and effective mobility. The Hall factor can be written as [15]

$$r = \frac{\langle \tau^2 \rangle}{\langle \tau \rangle^2} = \frac{\int_0^\infty \tau^2(E) \cdot E^{3/2} (\partial f_0 / \partial E) dE / \int_0^\infty E^{3/2} (\partial f_0 / \partial E) dE}{\left[\int_0^\infty \tau(E) \cdot E^{3/2} (\partial f_0 / \partial E) dE / \int_0^\infty E^{3/2} (\partial f_0 / \partial E) dE \right]^2}, \quad (3.4)$$

where τ is relaxation time of the conduction electron and f_0 is Fermi-Dirac distribution function. Although the Hall factor changes due to the energy dependence of the relaxation time, it is generally over 1. Therefore, the Hall mobility tends to be overestimated compared with the field-effect mobility. However it is also suggested that the field-effect mobility and Hall mobility show similar trend which is that the mobility increases with increasing the channel thickness. Although the influence of the misfit dislocation at the ZnO/YSZ interface becomes stronger, the results indicate that the field effect of ferroelectric polarization promotes the conduction close the P(VDF-TeFE)/ZnO interfaces and enhances the mobility.

The poling voltage dependence of the carrier transport properties of the P(VDF-TeFE)/ZnO heterostructures was investigated for the detail discussions of the effect of ferroelectric polarization on the carrier transport in the FeFETs. The measurement was performed on the 100 and 500 nm-thick FeFETs with a gate voltage of 0 V after poling treatments. Figure 3.12 shows the results of the Hall-effect measurements of the sample with the channel thickness of 500 nm. The poling voltage was varied from -40 to 40 V by

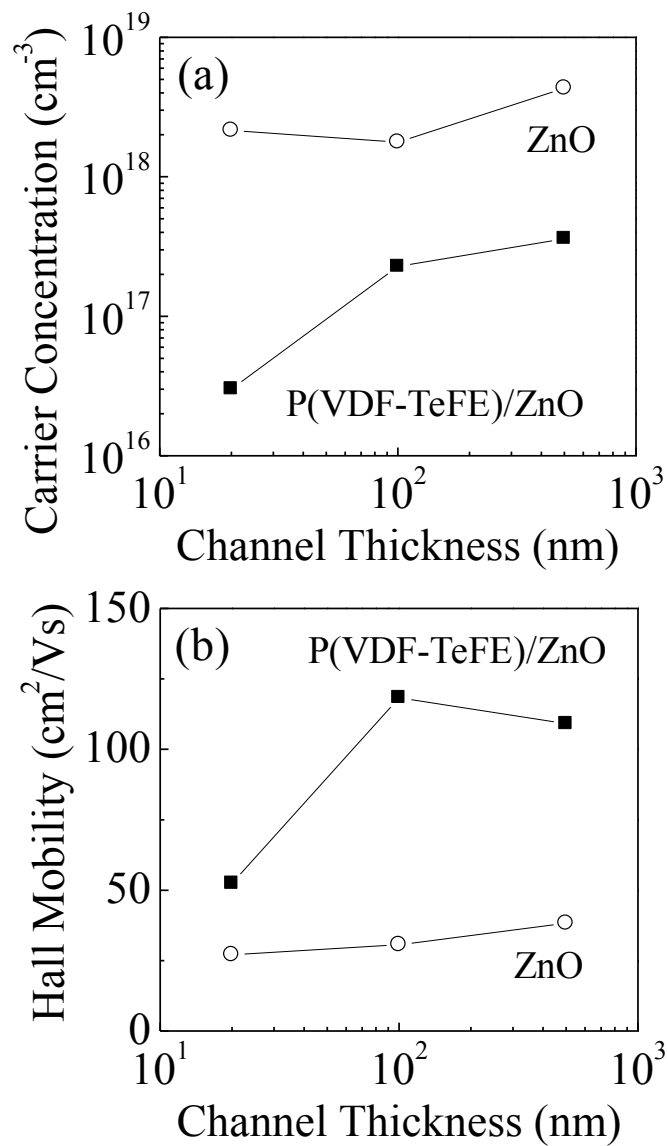


Fig. 3.11 The channel thickness dependence of the carrier concentration (a) and Hall mobility (b) of the ZnO films (open circles) and the P(VDF-TeFE)/ZnO/YSZ heterostructures (filled squares).

20 V step. The carrier concentration at the channel thickness of 500 nm, which is shown in Fig. 3.12(a), increases with increasing poling voltage from -40 to 40 V and shows counterclockwise hysteresis behavior. This behavior indicates the carrier modulation in the channel by the ferroelectric polarization. Figure 3.12(b) shows the Hall mobility at the channel thickness of 500 nm. While the carrier concentration is modulated as described above, the Hall mobility is almost constant against the poling voltage and is about $110 \text{ cm}^2 \cdot \text{V}^{-1} \cdot \text{s}^{-1}$, which is much higher than that of the ZnO film without the P(VDF-TeFE) layer ($38 \text{ cm}^2 \cdot \text{V}^{-1} \cdot \text{s}^{-1}$). The constant and high Hall mobility of 500 nm-thick FeFETs can be explained by the change in the conduction path and less depletion behaviors, as described above.

Figure 3.13(a) shows the carrier concentration at the channel thickness of 100 nm. The carrier concentration increases with increasing poling voltage. The absence of clear hysteretic behavior may be caused by the charge injection due to the existence of trapping states and the poling treatments at the high voltage above the coercive voltage. The Hall mobility of the 100-nm-thick channel sample is modulated by the ferroelectric polarization, as shown in Fig. 3.13(b). When the P(VDF-TeFE) layer is positively polarized, the Hall mobility increases to $125 \text{ cm}^2 \cdot \text{V}^{-1} \cdot \text{s}^{-1}$, which is higher than that for the 500 nm-thick channel sample. On the other hand, by negative poling, the Hall mobility decreases to below $5 \text{ cm}^2 \cdot \text{V}^{-1} \cdot \text{s}^{-1}$.

The sheet carrier concentration at the channel thickness of 500 nm is $2.8 \times 10^{13} \text{ cm}^{-2}$, which is larger than that at the channel thickness of 100 nm ($2.4 \times 10^{12} \text{ cm}^{-2}$). The sheet carrier concentration modulated by the remnant polarization of P(VDF-TeFE) ($2.7 \text{ } \mu\text{C}/\text{cm}^2$) was calculated to be approximately $1.7 \times 10^{13} \text{ cm}^{-2}$, which is larger than the sheet carrier concentration at the channel thickness of 100 nm and smaller than that at the

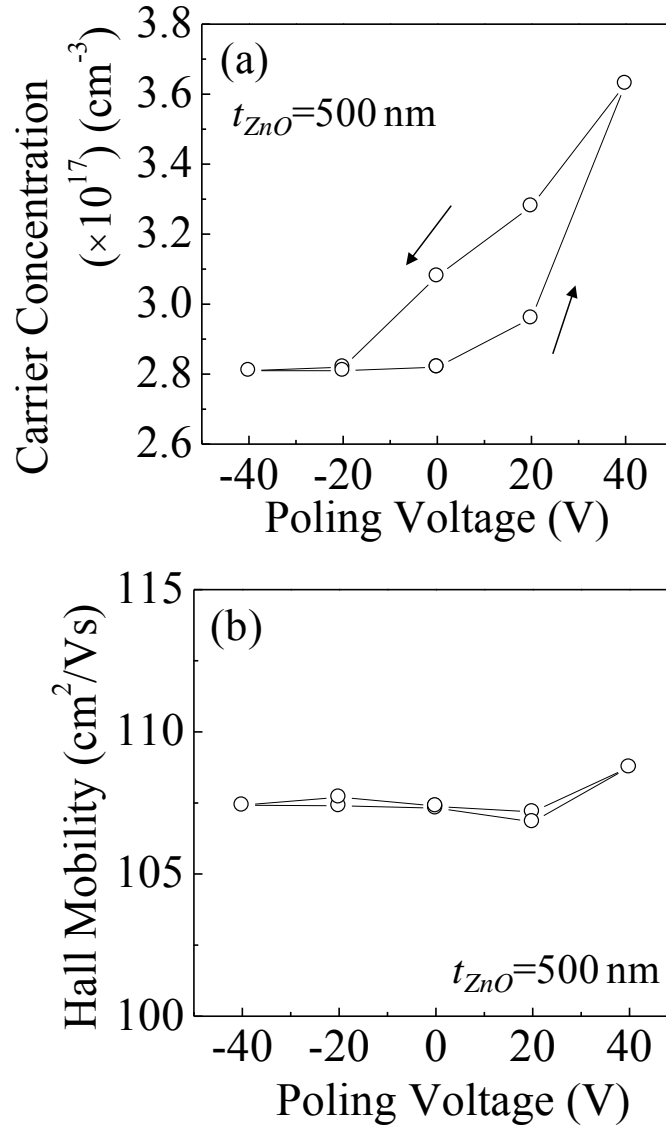


Fig. 3.12 The poling voltage dependence of the carrier concentration (a) and the Hall mobility (b) at the channel thickness of 500 nm.

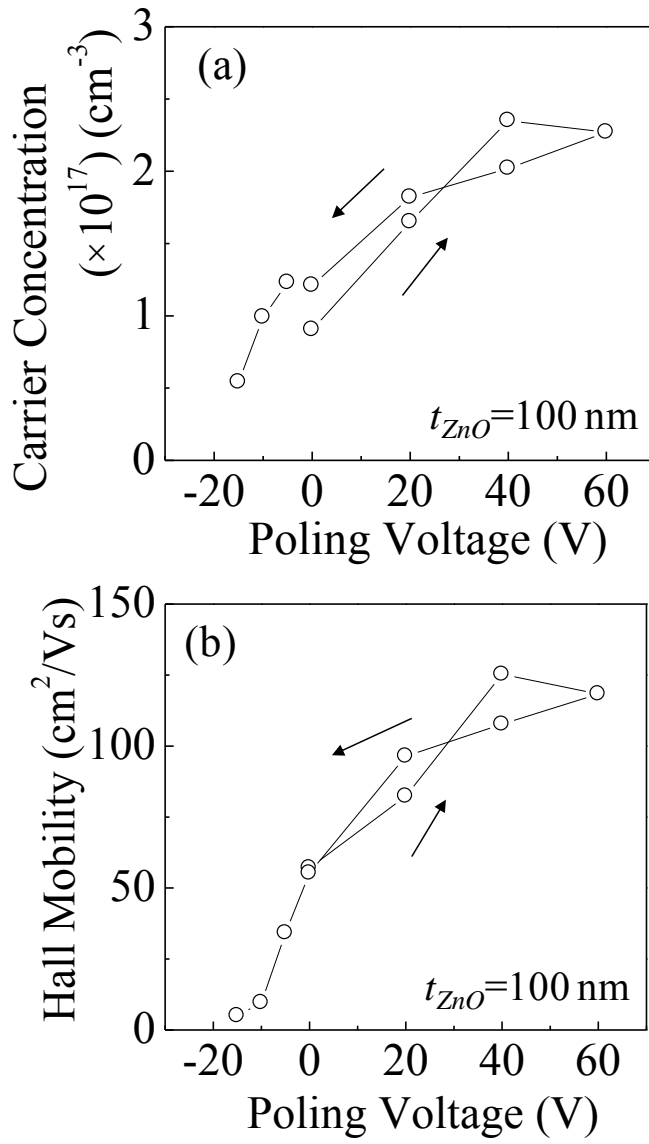


Fig. 3.13 The poling voltage dependence of the carrier concentration (a) and the Hall mobility (b) at the channel thickness of 100 nm.

channel thickness of 500 nm. The slight change in Hall mobility in the 500 nm-thick channel seems to indicate that the influence of the ferroelectric polarization is small owing to the larger amount of carriers. However, in the subsection 3.3.1 the Hall mobility of FeFETs with a thin channel (20 nm) was influenced by ferroelectric polarization even when the FeFETs have a high conductivity and carrier concentration (see Fig. 3.4). Thus, the effect of the ferroelectric polarization on the mobility is large in the region close to the ferroelectric/polar semiconductor interfaces. In the thick channel FeFETs, the ferroelectric polarization also accumulates or depletes the carriers near the ferroelectric/polar semiconductor interfaces. However, the carriers may flow over the whole channel layer under the weak influence of the ferroelectric polarization because the depletion width would be formed less than 50 nm which is much smaller than the channel thickness. In contrast, the carriers in thin channel FeFETs travel near the ferroelectrics/semiconductors interface. Therefore, in case of the thin channel FeFETs, the influence of the ferroelectric polarization on the carrier transport becomes strong and the Hall mobility can be modulated by the poling treatments.

The poling voltage dependence of the carrier transport properties of the FeFETs reveals that the carrier accumulation by the ferroelectric polarization can increase the mobility. To investigate the changes in the carrier scattering mechanisms, the temperature dependence of the carrier transport properties was characterized. In the 100 nm-thick channel FeFETs, two poling states were formed by applying positive and negative voltages of ± 50 V, and the Hall-effect measurements were carried out at temperatures ranging from 80 to 300 K. Figure 3.14(a) shows the results for the carrier concentration. When the P(VDF-TeFE) layer is positively polarized, the carriers are accumulated owing to the ferroelectric polarization. Thus, the carrier concentration at positive poling is larger than that at negative poling in the whole temperature range. This result suggests that two

distinct poling states were kept during the measurements. The Hall mobility shown in Fig. 3.14(b) increases when the P(VDF-TeFE) layer is positively polarized, especially below 200 K. The difference in the temperature dependence of the Hall mobility between the two poling states at a low temperature may be caused by the ionized impurities. The ionized impurities scatter carriers through their screened Coulomb potential, and the associated mobility is proportional to two-thirds of temperature [15–17]. Additionally, the field effect is known to reduce the scattering effect of the Coulomb potential [18, 19]. From the results, it is suggested that the carriers accumulated owing to the ferroelectric polarization screen the influence of the Coulomb potential from the ionized impurities. Thus, it is revealed that the mobility of the FeFETs is increased through the reduction of the ionized impurity scattering by the field effect of the ferroelectric polarization without an applied gate voltage.

3.4 Conclusions

The electronic transport properties of CP-type FeFETs with P(VDF-TeFE)/ZnO heterostructures were investigated. To clarify the effect of ferroelectric polarization on the carrier transport in the FeFETs, the Hall-effect measurements with the poling treatments were carried out to the various channel thicknesses FeFETs. While the carrier modulation effect was observed in all the samples, the modulation of the Hall mobility is obtained in FeFETs with the channel thicknesses thinner than 100 nm. The results indicate that the modulation effect of mobility is confined in the region close to ferroelectric/semiconductor interfaces and this means the ferroelectric polarization strongly influences at the interfaces. It is also suggested that the electronic transport in the ZnO thin films is disturbed by the formation of the multidomain structure of ferroelectrics. However this effect would not be matter because the enhancement of the mobility by ferroelectric polarization is rather

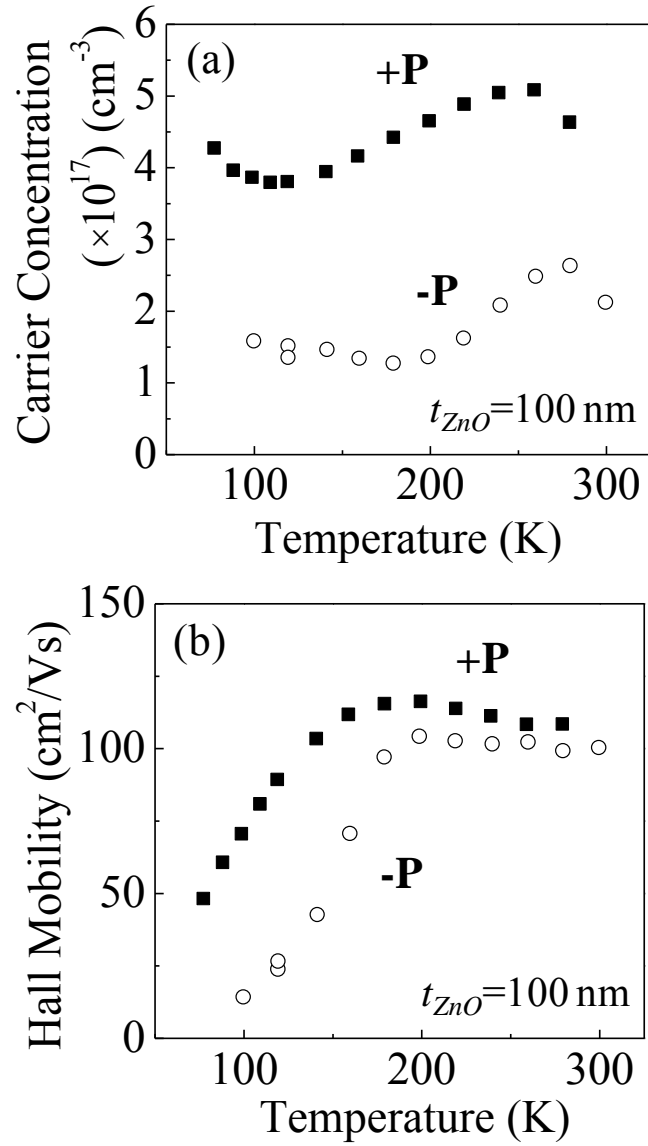


Fig. 3.14 The temperature dependence of the carrier concentration (a) and the Hall mobility (b) at the channel thickness of 100 nm. The results at the positive (+P) and the negative (-P) poling show filled squares and open circles, respectively.

prominent and the disturbing effect can be reduced if the ferroelectric are the fully-polarized. As a result of the temperature dependence of the Hall measurements with positive and negative poling, the modulation effect of the Hall mobility owing to ferroelectric polarization was found to be the reduction of the ionized impurity scattering. Thus, it is concluded that the ferroelectric polarization can enhance the mobility by screening the potential of impurities through the field-effect of the ferroelectric polarization.

References

- [1] T. Fukuma, K. Kobayashi, T. Horiuchi, H. Yamada, and K. Matsushige, *Jpn. J. Appl. Phys.* **39**, 3830 (2000).
- [2] S. N. Fedosov, A. E. Sergeeva, G. Eberle, and W. Eisenmenger, *J. Phys. D: Appl. Phys.* **29**, 3122 (1996).
- [3] Z. Y. Wang, K. H. Su, H. Q. Fan, and Z. Y. Wen, *Polymer* **48**, 7145 (2007).
- [4] T. Kanashima, K. Yabe, and M. Okuyama, *Jpn. J. Appl. Phys.* **51**, 02BK06 (2012).
- [5] Y. Kaneko, H. Tanaka, and Y. Kato, *Jpn. J. Appl. Phys.* **48**, 09KA19 (2009).
- [6] D. Shahrjerdi, J. Nah, B. Hekmatshoar, T. Akyol, M. Ramon, E. Tutuc, and S. K. Banerjee, *Appl. Phys. Lett.* **97**, 213506 (2010).
- [7] P. D. Kirsch, M. A. Q.- Lopez, H.-J. Li, Y. Senzaki, J. J. Peterson, S. C. Song, S. A. Krishnan, N. Moumen, J. Barnett, G. Bersuker, P. Y. Hung, B. H. Lee, T. Lafford, Q. Wang, D. Gay, and J. G. Ekerdt, *J. Appl. Phys.* **99**, 023508 (2006).
- [8] C. G. Van de Walle, *Phys. Rev. Lett.* **85**, 1102 (2000).
- [9] Y. Wang, B. Meyer, X. Yin, M. Kunat, D. Langenberg, F. Traeger, A. Birkner, and C. Woll, *Phys. Rev. Lett.* **95**, 266104 (2005).

- [10] D.C. Look, H.L. Mosbacker, Y. M. Strzhemechny, and L. J. Brillson, *Superlattices Microstruct.* **38**, 406 (2005).
- [11] S. Sakamoto, T. Oshio, A. Ashida, T. Yoshimura, and N. Fujimura, *Appl. Surf. Sci.* **254**, 6248 (2008).
- [12] D. C. Look, and R. J. Molnar, *Appl. Phys. Lett.* **70**, 3377 (1997).
- [13] H. Tampo, A. Yamada, P. Fons, H. Shibata, K. Matsubara, K. Iwata, S. Niki, K. Nakahara, and H. Takasu, *Appl. Phys. Lett.* **84**, 4412 (2004).
- [14] S. M. Sze, and K. K. Ng, *Physics of Semiconductor Devices*, 3rd ed. (Wiley, New York, 2007) p. 308.
- [15] D. C. Look, *Electrical Characterization of GaAs Materials and Devices* (Wiley, New York, 1989) p. 54 and 76.
- [16] K. Hess, *Appl. Phys. Lett.* **35**, 484 (1979).
- [17] D. C. Look, D. C. Reynolds, J. R. Sizelove, R. L. Jones, C. W. Litton, G. Cantwell, and W. C. Harsch, *Solid State Commun.* **105**, 399 (1998).
- [18] S. Takagi, A. Toriumi, M. Iwase, and H. Tango, *IEEE Trans. Electron Devices* **41**, 2357 (1994).
- [19] S. V. Vandeboeck, E. F. Crabbe, B. S. Meyerson, D. L. Harnage, P. J. Restle, J. M. C. Stork, A. C. Megdanis, C. L. Stanis, A. A. Bright, G. M. W. Kroesen, and A. C. Warren, *IEEE Electron Device Lett.* **12**, 447 (1991).

Chapter 4: Effect of Spontaneous Polarization of Polar Semiconductor on Electrical Properties of Poly(vinylidene fluoride-trifluoroethylene)/ZnO Heterostructures

4.1 Introduction

In this chapter, the effect of the spontaneous polarization of the polar semiconductor on the electrical properties of the ferroelectric/polar semiconductor heterostructures was focused. P(VDF-TrFE) was employed as the ferroelectric layer. P(VDF-TrFE) is the typical organic ferroelectric which can be crystallized at a temperature below 150°C [1, 2] same as P(VDF-TeFE). Moreover, the crystallization of P(VDF-TrFE) is much easier than P(VDF-TeFE) because P(VDF-TrFE) has higher melting temperature, which is higher than the ferroelectric-paraelectric transition temperature. Thus the heterostructures using P(VDF-TrFE) and the two crystallographic polarities of O- and Zn-polar ZnO were formed.

The electrical properties of the P(VDF-TrFE)/O- and Zn-polar ZnO heterostructures were revealed. Moreover, the XPS measurements were made and to determine the band alignments of the P(VDF-TrFE)/O- and Zn-polar ZnO heterostructures, XPS measurements were carried out using synchrotron x-ray. The effect of the spontaneous polarization on the electrical properties of the ferroelectric/polar semiconductor heterostructures is discussed with the results of the band configurations of the P(VDF-TrFE)/ZnO heterostructures.

4.2 Experimental procedures

Thick P(VDF-TrFE) films (85 nm) and thin P(VDF-TrFE) (8 nm)/O- and Zn-polar ZnO heterostructures were made for the XPS measurements, and thick P(VDF-TrFE) (85

nm)/O- and Zn-polar ZnO were made to investigate the electrical properties. Double-polished ZnO single-crystalline substrates were used to obtain the distinct crystallographic polarities of O-polar ($000\bar{1}$) and Zn-polar (0001) faces. These substrates were processed with HF chemical etching and organic cleaning. After that, annealing treatment at a temperature of 950°C in air was performed to obtain flat surfaces. The surface morphologies of the O- and Zn-polar ZnO are shown in Fig. 4.1. Although small surface imperfections from the etching process exist on the Zn-polar ZnO surface, step and terrace structures can be observed on both polar surfaces. P(VDF-TrFE) with a VDF/TrFE molar ratio of 75/25 was dissolved into diethyl carbonate. The thickness of the P(VDF-TrFE) films was controlled by adjusting the concentration of the solutions to 1 and 3 wt.% for thin (8 nm) and thick (85 nm) films, respectively. The P(VDF-TrFE) films were spin-coated on O- and Zn-polar ZnO and Pt/Ti/SiO₂/Si substrates. The annealing treatments were performed at 120°C to crystallize the P(VDF-TrFE) layers. Top electrodes of Au and backside ohmic electrodes of Au/Ti were formed on the samples for the electrical measurements by an EB evaporation method. To calibrate the energy shift caused by the charge effect during the XPS measurements, Au was deposited on the samples for the XPS analysis by PLD at room temperature.

4.3 Results and discussion

4.3.1 Electrical properties of poly(vinylidene fluoride-trifluoroethylene)/O- and Zn-polar ZnO heterostructures

The C-V characteristics of the P(VDF-TrFE)/O- and Zn-polar ZnO are shown in Fig. 4.2. The measurements were performed by applied a bias voltage swept between -15

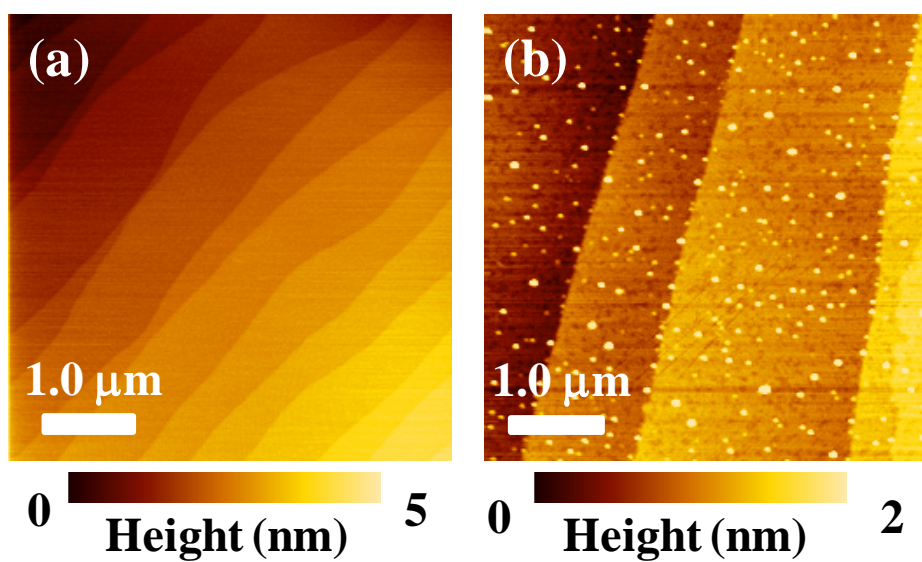


Fig. 4.1 The surface morphologies of the O- (a) and Zn-polar ZnO (b).

and 15 V. The AC signal was 10 mV and 10 kHz. Butterfly-type C - V curves originating from the ferroelectric polarization reversal were observed in both the P(VDF-TrFE)/O- and Zn-polar ZnO. A distinct difference in the C - V curves was found at the negative voltage side, while the C - V curves at the positive voltage side, which correspond to the dielectric properties of the P(VDF-TrFE) layers, show similar results. The distinct decrease in the capacitance of the P(VDF-TrFE)/O-polar ZnO indicates the formation of a depletion layer attributed to the ferroelectric polarization reversal. However, P(VDF-TrFE)/Zn-polar ZnO shows little decrease in capacitance even at -15 V. The depletion widths of P(VDF-TrFE)/O- and Zn-polar ZnO calculated from the capacitances at ± 15 V are 280 and 33 nm, respectively.

Figure 4.3 shows the P - V characteristics of P(VDF-TrFE)/O- and Zn-polar ZnO. The hysteresis loops denote the ferroelectricity of P(VDF-TrFE) on ZnO. The remnant and the saturated polarizations and the coercive voltage are $3.9 \mu\text{C}/\text{cm}^2$, $4.5 \mu\text{C}/\text{cm}^2$, and 7.0 V for P(VDF-TrFE)/O-polar ZnO; and $4.1 \mu\text{C}/\text{cm}^2$, $5.3 \mu\text{C}/\text{cm}^2$, and 8.0 V for P(VDF-TrFE)/Zn-polar ZnO, respectively. The formation of the depletion layer in ZnO is indicated by the changes in the slope of the saturation region of the P - V characteristics, which corresponds to the capacitance of the heterostructures. The calculated relative permittivities of the P(VDF-TrFE)/O- and Zn-polar ZnO are 7.2 and 8.7 at the positive side and 1.9 and 5.9 at the negative side, respectively. The apparent permittivity of O-polar ZnO in the negative voltage region is lower than those of the others, which corresponds to the results of the C - V measurements. To further explore the influence of spontaneous polarization on the electrical properties in detail, the band diagram, which reflects the charge variation at the heterointerface, was analyzed using the XPS measurements.

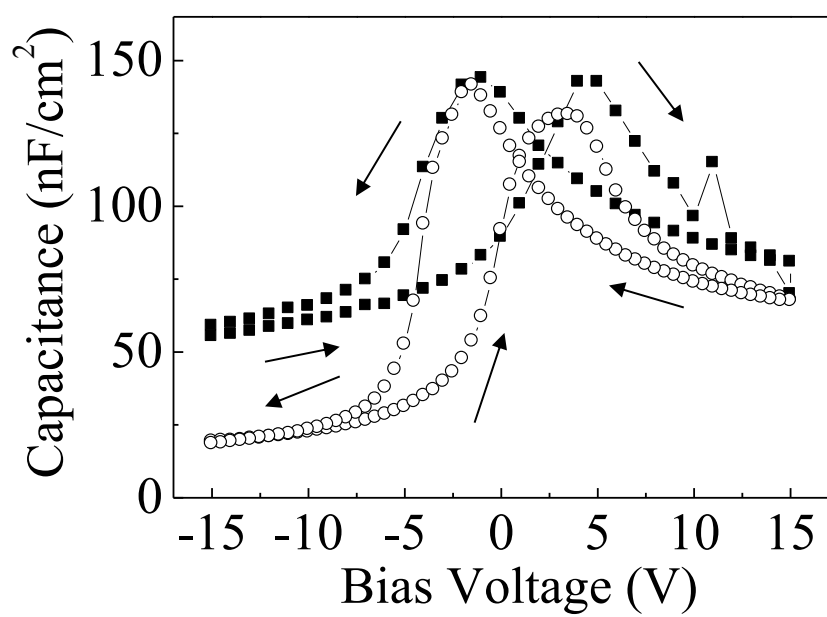


Fig. 4.2 The C-V characteristics of the P(VDF-TrFE)/O- (open circles) and Zn-polar ZnO (filled squares).

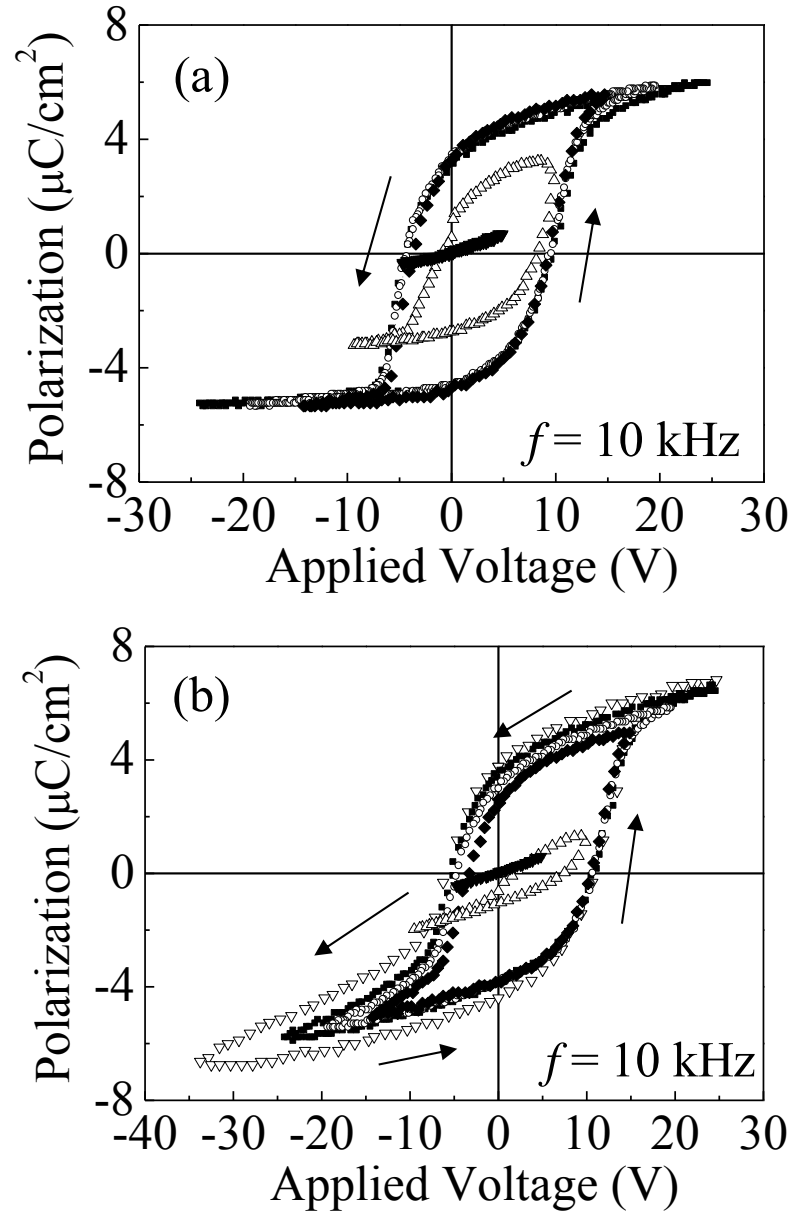


Fig. 4.3 The P - V characteristics of the P(VDF-TrFE)/O- (a) and Zn-polar ZnO (b) measured at 10 kHz.

4.3.2 Analysis of band alignments of heterostructures with poly(vinylidene fluoride-trifluoroethylene)/O- and Zn-polar ZnO heterostructures

ZnO substrates, the P(VDF-TrFE) thick film (85 nm) on a Pt/Ti/SiO₂/Si substrate, and the P(VDF-TrFE)/ZnO heterostructures with the different ZnO polarities were used to reveal the energy band relationships between P(VDF-TrFE) and ZnO. Figure 4.4 shows the results of the XPS measurements, which are the core level (CL) spectra of Zn 2p_{3/2} and F 1s, and valence band edges spectra. The measurements were performed with the energy steps of 0.08 eV, which denote the energy resolution of each spectrum. All spectra were calibrated using Au 4f_{7/2} CL peak, which was assumed to be 83.8 eV. The CL spectra were fitted using the Voigt (mixed Lorentzian-Gaussian) functional form and the Shirley background. The binding energies of each CL were determined from the positions of maximum intensity of the fitted lines. The valence band maximum (VBM) was determined from linear extrapolation of valence band edges to the base lines to account for the instrument resolution-induced tail [3]. The analysis was performed with the assumption that the highest occupied molecular orbital (HOMO) level corresponds to the VBM.

The band alignment at the heterointerfaces of the P(VDF-TrFE)/ZnO can be analyzed by calculating the valence band offset (E_{VBO}) by using the following equation [4]:

$$E_{VBO} = (E_{F1s}^{PVDf} - E_V^{PVDf}) - (E_{Zn2p}^{ZnO} - E_V^{ZnO}) - \Delta E_{CL}, \quad (4.1)$$

where ΔE_{CL} is the separation in the binding energy of the CL spectra of F 1s and Zn 2p_{3/2} at the P(VDF-TrFE)/ZnO heterointerfaces. The former two components determined from the P(VDF-TrFE) thick film and ZnO substrate. From the CL and valence band edge spectra of P(VDF-TrFE) and ZnO (Fig. 4.4), $(E_{F1s}^{PVDf} - E_V^{PVDf})$ and $(E_{Zn2p}^{ZnO} - E_V^{ZnO})$ were determined to be 687.4 and 1019.9 eV, respectively. The ΔE_{CL} of the P(VDF-TrFE)/O- and

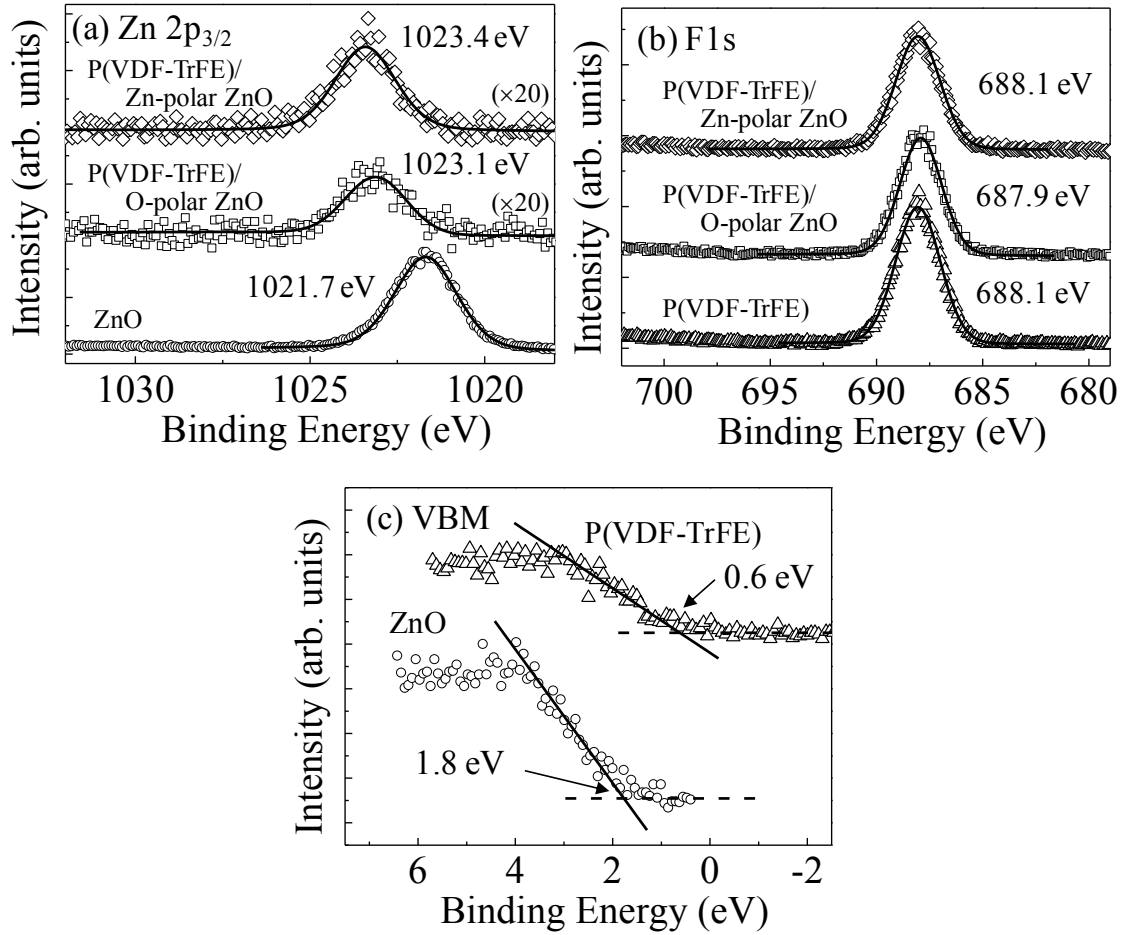


Fig. 4.4 The CL spectra of Zn 2p_{3/2} (a) and F 1s (b), and the valence band edge spectra (c). The measured results of the ZnO substrate (circles), the P(VDF-TrFE) film (triangles), the P(VDF-TrFE)/O- (squares) and Zn-polar ZnO (rhomboids) heterostructures are shown. The solid lines are the fitted line using the Voigt function (a, b) and the linear extrapolation forms (c), and the dashed lines are base lines.

Zn-polar ZnO were determined to be 335.2 and 335.4 eV, respectively. Therefore, the E_{VBO} of the P(VDF-TrFE)/O- and Zn-polar ZnO becomes 2.7 and 2.9 eV, respectively, as schematically shown in Fig. 4.5 (a) and (b). In this scheme, the band gap energies of the P(VDF-TrFE) and ZnO are assumed as 5.6 [5, 6] and 3.4 eV, respectively. The results indicate that the heterostructures with the P(VDF-TrFE) and ZnO have a staggered band alignment with a large E_{VBO} .

In this section, the origin of the observed differences in the electrical properties of the heterostructures with the different crystallographic polarities of ZnO (Figs. 4.2, 4.3) is discussed. The P(VDF-TrFE)/Zn-polar ZnO shows rather little depletion compared with the P(VDF-TrFE)/O-polar ZnO. The carrier concentrations of these two samples, estimated from the maximum depletion width, are 3.5×10^{16} and $2.7 \times 10^{18} \text{ cm}^{-3}$, respectively. Because the Hall-effect measurement indicates that the O- and Zn-polar ZnO substrates have nearly the same amount of carriers, at 1.1×10^{17} and $9.8 \times 10^{16} \text{ cm}^{-3}$, respectively, it is suggested that the differences in the electrical properties originate from the polarization charges and band lineup. Figure 4.5 (c)-(f) show schematic images of the band diagram of the heterointerfaces of P(VDF-TrFE)/ZnO, taking into account the direction of polarizations. When the polarization of P(VDF-TrFE) directs downward (Fig. 4.5 (c) and (e)), both polarities of ZnO at the heterointerfaces form accumulation states and bend the energy band downward. Conversely, when the polarization of P(VDF-TrFE) aligns upward (Fig. 4.5 (d) and (f)), both of the ZnO layer are depleted and bend the energy band upward. The influence of the spontaneous polarization of ZnO is observed in the differences in the surface potential of ZnO. In the case of the accumulation states, the O-polar surface requires a large amount of electrons to compensate the head-to-head polarizations, while the Zn-polar surface needs less electrons because of the charge compensation between the polarizations. ZnO is a typical n-type semiconductor, so the interface charge is neutralized

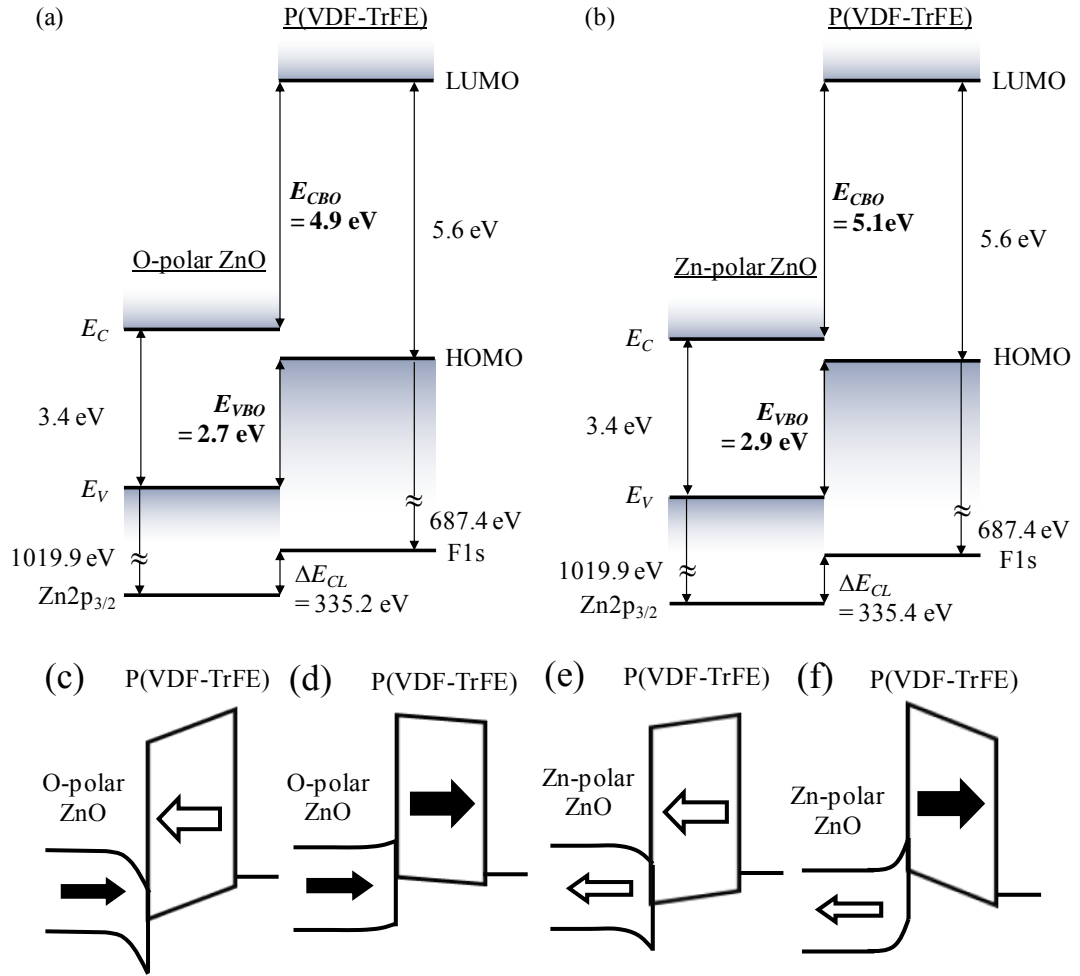


Fig. 4.5 The energy band diagrams of the P(VDF-TrFE)/O- (a) and Zn-polar ZnO (b) as determined by XPS measurements. Schematic images of the band diagram of the P(VDF-TrFE)/O- (c, d) and Zn-polar ZnO (e, f) considering the direction of the polarization of the P(VDF-TrFE) layers as downward (c, e) and upward (d, f) are shown.

by electrons. When ZnO is depleted, conversely, the O-polar surface holds charge compensation because of the polarizations and the Zn-polar surface requires a large amount of holes to compensate the mismatched charges arising from the tail-to-tail geometry of the polarizations. Because of the lack of p-type carriers in the ZnO layer, the Zn-polar ZnO generates a high surface potential to induce holes. As a result, a high electric field is applied to the P(VDF-TrFE) layer. Although P(VDF-TrFE) has an insulating nature, the XPS spectra of the P(VDF-TrFE) film shown in Fig. 4.4 (c) indicates the Fermi level in P(VDF-TrFE) exists near the HOMO level, up to 0.6 eV. Figure 4.6(a) shows a thermal activated current of the P(VDF-TrFE)/Zn-polar ZnO at temperatures ranging from 40 to 130°C. It was found that a large amount of current flows at the P(VDF-TrFE)/ZnO heterointerfaces. The charge density of P(VDF-TrFE)/ZnO, which includes trapping holes at P(VDF-TrFE) surface, is estimated as $5.5 \times 10^{14} \text{ cm}^{-2}$ from an integral of the current (blue region in Fig. 4.6(a)). Activation energy (E_a) of the thermal activated current is analyzed using Arrhenius plot, which is shown in Fig. 4.6(b). E_a was determined to be 0.84 eV. The value of E_a is close to the energy difference between the Fermi level and VBM of the P(VDF-TrFE) (0.6 eV), which is determined from valence band edge spectra of P(VDF-TrFE) thick film (Fig. 4.4(c)). Thus, it is suggested that holes are generated in P(VDF-TrFE) and screen the electrical contribution of the ZnO layer. This explanation is consistent with the difference in depletion behaviors of P(VDF-TrFE)/O- and Zn-polar ZnO. The results presented in this paper indicate that the relationship between the interface charge induction by spontaneous polarization and the energy band alignment with a staggered and large gap has a significant impact on the electrical properties of heterostructures of P(VDF-TrFE) and ZnO.

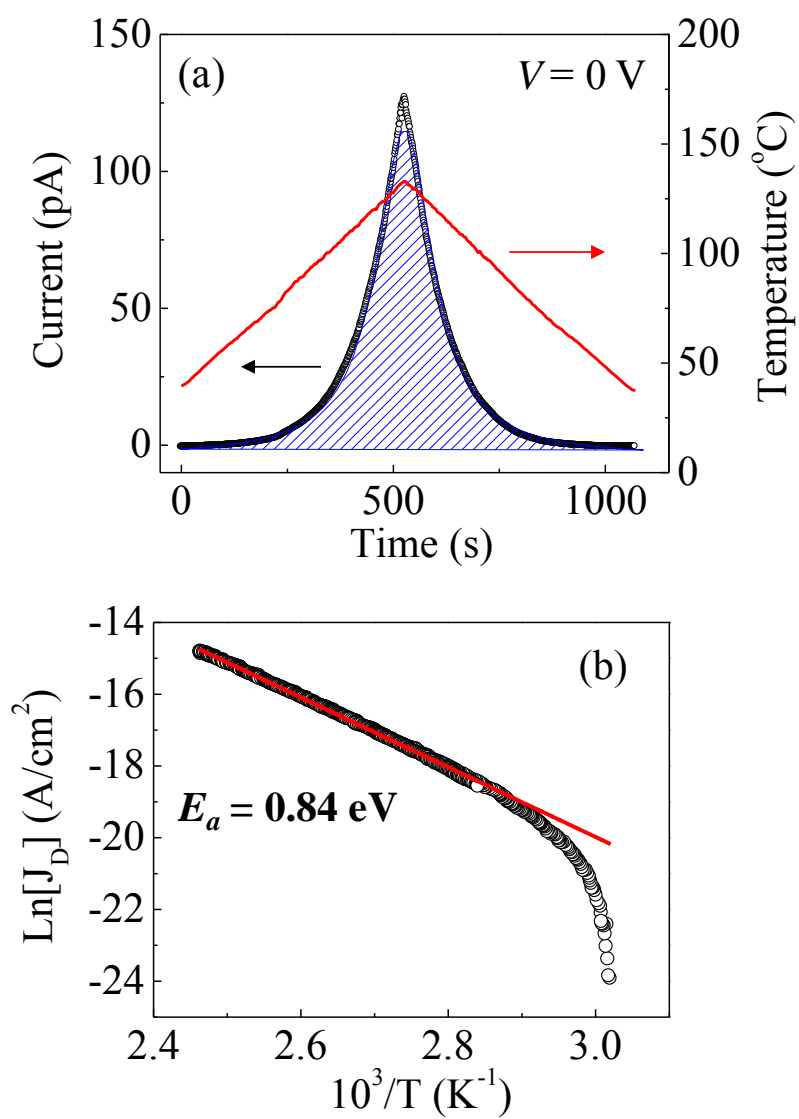


Fig. 4.6 (a) The thermal activated current of the P(VDF-TrFE)/Zn-polar ZnO. (b) The Arrhenius plot of the thermal activated current.

4.4 Conclusions

The electrical properties of the heterostructures of P(VDF-TrFE)/O- and Zn-polar ZnO were examined, with the band configuration of the heterointerfaces determined by the XPS measurements. The heterostructure with Zn-polar ZnO shows a weaker depletion than does the O-polar ZnO. The differences in the electrical properties arise from the carrier generation at the heterointerfaces which is not attributed to the semiconducting nature of ZnO. CL XPS spectra indicate that the band alignments of both the P(VDF-TrFE)/O- and Zn-polar ZnO were staggered band configurations with a large E_{VBO} ranging from 2.7 to 2.9 eV. It is suggested that the spontaneous polarization of ZnO influences the electrical properties through carrier generation at the heterointerfaces for the interface charge neutralization related to the large E_{VBO} .

References

- [1] H. Kodama, Y. Takahashi, and T. Furukawa, Jpn. J. Appl. Phys. **38**, 3589 (1999).
- [2] K. Tashiro, H. Kaito, and M. Kobayashi, Polymer **33**, 2915 (1992).
- [3] R. Q. Zhang, P. F. Zhang, T. T. Kang, H. B. Fan, X. L. Liu, S. Y. Yang, H. Y. Wei, Q. S. Zhu, and Z. G. Wang, Appl. Phys. Lett. **91**, 162104 (2007).
- [4] E. A. Kraut, R. W. Grant, J. R. Waldrop, and S. P. Kowalczyk, Phys. Rev. Lett. **44**, 1620 (1980).
- [5] D. Mandal, K. Henkel, K. Muller, and D. Schmeiber, Bull. Mater. Sci. **33**, 457 (2010).
- [6] J. Choi, P. A. Dowben, S. Pebley, A. V. Bune, S. Ducharme, V. M. Fridkin, S. P. Palto, and N. Petukhova, Phys. Rev. Lett. **80**, 1328 (1998).

Chapter 5: Crystal Growth of (111) (Ba_{1-x}Ca_x)TiO₃ on (000 $\bar{1}$) ZnO Substrates for Lattice Matched Heterostructures with Ferroelectrics and Polar Semiconductors

5.1 Introduction

Heteroepitaxial growth of functional oxides on semiconductors is an important technology for the development of novel devices. The development of thin film technologies for these materials has enabled high-quality epitaxial films of these perovskite ferroelectrics to be realized not only on perovskite crystals but also on conventional semiconductors such as Si and GaAs [1–3]. It has been suggested in several reports that the heteroepitaxial growth of ferroelectrics on semiconductors can be eased by using buffer layers, which lead to a reduction in the surface energy that is attributed to the interfacial bonds and the lattice strain that arises from lattice mismatches between the films and the substrates and any defects [4, 5]. The use of the buffer layers, however, is not suitable for certain devices because of the increased numbers of defects and the associated depolarization field. It is therefore important to develop compatible heteroepitaxial structures of ferroelectrics and semiconductors based on direct stacking. Heteroepitaxy with a combination of oxide materials is one appropriate solution to produce highly crystalline ferroelectrics with a clean heterointerface [6].

In this chapter, the lattice matched heterostructures with BCT and ZnO is focused. It is known that Ca substitution in BTO reduces the lattice volume with no degradation of ferroelectricity because of the anomalous displacements of Ca and Ti off-centering [7–9]. The (111)-oriented BCT films on the (000 $\bar{1}$) ZnO surface have two possible in-plane

epitaxial relationships of $[110]\text{BCT} \parallel [10\bar{1}0]\text{ZnO}$ and $[112]\text{BCT} \parallel [10\bar{1}0]\text{ZnO}$. The lattice mismatch of the former relationship ($f_b = (\sqrt{2}a_{\text{BCT}} - \sqrt{3}a_{\text{ZnO}})/\sqrt{3}a_{\text{ZnO}}$) can be adjusted to 0%, while that of the latter relationship ($f_b = (a_{\text{BCT}}/\sqrt{2} - a_{\text{ZnO}})/a_{\text{ZnO}}$) is more than -12%. However, many reports on heterostructures comprising perovskite ferroelectrics and wurtzite-type semiconductors such as ZnO and GaN describe the polycrystalline nature of the ferroelectrics and the in-plane epitaxial relationships with large lattice mismatches [10–12]. These facts indicate that the influence of the chemical interaction energy of the interfacial bonds is stronger than the lattice mismatch at the perovskite ferroelectric/wurtzite-type semiconductor interface [12]. In this chapter, the epitaxial growth of (111) BCT films on ZnO substrates is investigated and the mechanism for formation of (111)BCT/(000 $\bar{1}$) ZnO heterointerfaces is discussed.

5.2 Experimental procedures

BCT thin films were deposited on (000 $\bar{1}$) ZnO substrates by PLD. A KrF excimer laser ($\lambda=248$ nm) with laser power density of 0.4 J/cm^2 and a repetition rate of 1 Hz was used. The ZnO substrates were cleaned and chemically etched using a HF solution with a concentration of 10^{-4} wt.%. Then, the substrates were annealed at 1000°C in air. A BCT ceramic target with Ca content of 0.10 was fabricated in an electric muffle furnace. The target to substrate distance was set at 30 mm during deposition. The BCT films were grown at a substrate temperature of 600°C and an oxygen pressure of 1×10^{-1} Torr. The deposition rate was 0.01 nm/s. Structural characterization of the resulting films was carried out using in-situ reflective high energy electron diffraction (RHEED) and XRD measurements.

5.3 Results and discussion

The XRD 2θ - ω profile of a BCT thin film deposited on the ZnO substrate is shown in Fig. 5.1. The results indicate that only (001) BCT is grown on ZnO. Figure 5.2 shows the RHEED patterns of the BCT film at the $[10\bar{1}0]$ and $[11\bar{2}0]$ azimuths for ZnO. The patterns show similar diffractions, low intensities, and halo-like structures, which indicates that the BCT was not grown epitaxially and had low crystallinity. Despite the fact that BCT thin film growth on ZnO was investigated at various temperatures in the range from 400 to 800°C, oxygen pressures ranging from 1.0×10^{-4} to 1.0×10^{-1} Torr, and under various laser power conditions, (111) BCT could not be obtained.

To change the atomic arrangement of the ZnO substrate surface, a $(\sqrt{3} \times \sqrt{3})$ R30° reconstructed ZnO substrate surface was focused. The reconstructed surface forms a stable surface throughout the adsorption or removal of atoms at the top-most surface. Hove and Leysen reported the reconstruction of (0001) and $(000\bar{1})$ ZnO with annealing in a 760 Torr oxygen atmosphere at 600°C. They suggested that the reconstruction represents simple chemisorption on the $(000\bar{1})$ surface, but on the (0001) surface, oxygen took part at least partially in the crystal stabilization [13]. Recently, King et al. demonstrated the formation of a stable reconstructed surface of $(000\bar{1})$ ZnO by annealing in an ultra-high vacuum system [14]. They suggested that the surface reconstruction, which originates from oxygen vacancies, can be realized using a hydrogen-free atmosphere. In addition, Li et al. investigated the formation energy of the reconstructed surface [15]. From ab initio calculations, the $(\sqrt{3} \times \sqrt{3})$ R30° reconstructed surface with oxygen vacancies is shown to be stable at high temperatures with a poor oxygen atmosphere. The ZnO substrates were therefore annealed in a vacuum chamber at 860°C and at an oxygen pressure of 1.0×10^{-2}

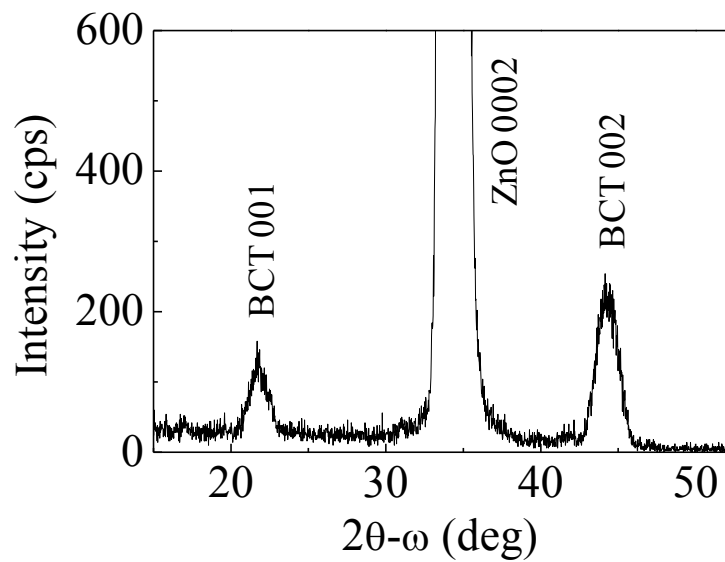


Fig. 5.1 XRD 2θ - ω profile of the BCT/ZnO heterostructure.

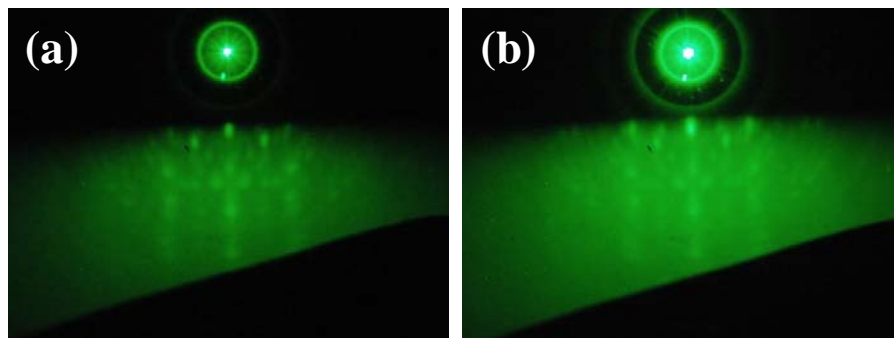


Fig. 5.2 RHEED patterns of the BCT thin films deposited on ZnO at (a) the $[10\bar{1}0]$ azimuth and (b) the $[11\bar{2}0]$ azimuth for ZnO.

Torr to form the stable $(\sqrt{3} \times \sqrt{3})R30^\circ$ reconstructed surface. RHEED patterns measured before and after annealing are shown in Fig. 5.3. The streak patterns indicate the smooth ZnO surfaces. The additional streak patterns in the $[10\bar{1}0]$ azimuth and the invariance patterns in the $[11\bar{2}0]$ azimuth indicate the formation of the reconstructed surface on $(000\bar{1})$ ZnO.

BCT films were deposited on the reconstructed surface under the same conditions that were used for the deposition of the film shown in Figs. 5.1 and 5.2. The RHEED patterns of the BCT on the reconstructed surface are shown in Fig. 5.4. The RHEED patterns at the $[110]$ and $[112]$ azimuths for BCT are observed at the $[10\bar{1}0]$ and $[11\bar{2}0]$ azimuths for ZnO, respectively. The patterns at the $[110]$ azimuth for BCT are also observed at the $[11\bar{2}0]$ azimuth of ZnO, which indicates the existence of a 30° rotation domain. Figure 5.5 shows the out-of-plane and in-plane XRD profiles of the BCT film on the reconstructed surface. As shown, a (111) BCT film is grown on the ZnO with the reconstructed surface. The ϕ scan for BCT (110) shows 12 peaks, which can be divided into higher and lower intensity peaks. The peak positions of the higher peaks corresponding to the six peaks of ZnO $(11\bar{2}2)$ indicates the dominant epitaxial relationship of $(111)[110]\text{BCT} \parallel (000\bar{1})[10\bar{1}0]\text{ZnO}$, although the undesirable domains with $(111)[112]\text{BCT} \parallel (000\bar{1})[10\bar{1}0]\text{ZnO}$ are also formed. These results are consistent with the RHEED patterns shown in Fig. 5.4.

The crystal growth mechanism of (111) BCT on the $(\sqrt{3} \times \sqrt{3})R30^\circ$ reconstructed ZnO surface must also be discussed. The reconstructed surface is believed to

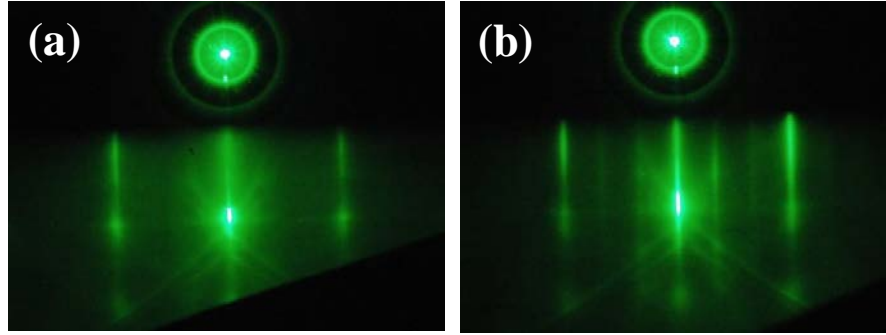


Fig. 5.3 RHEED patterns of (a) the unreconstructed and (b) the $(\sqrt{3} \times \sqrt{3})R30^\circ$ reconstructed surfaces of ZnO. The incident azimuth for ZnO was $[10\bar{1}0]$.

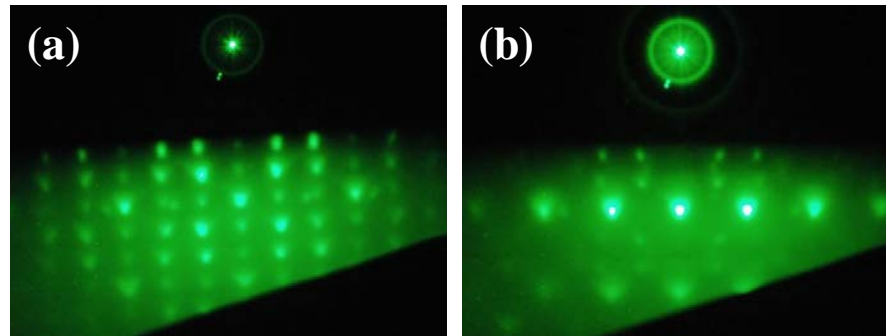


Fig. 5.4 RHEED patterns of BCT thin films deposited on the reconstructed surfaces of ZnO. The incident azimuth for ZnO was (a) $[10\bar{1}0]$ and (b) $[11\bar{2}0]$.

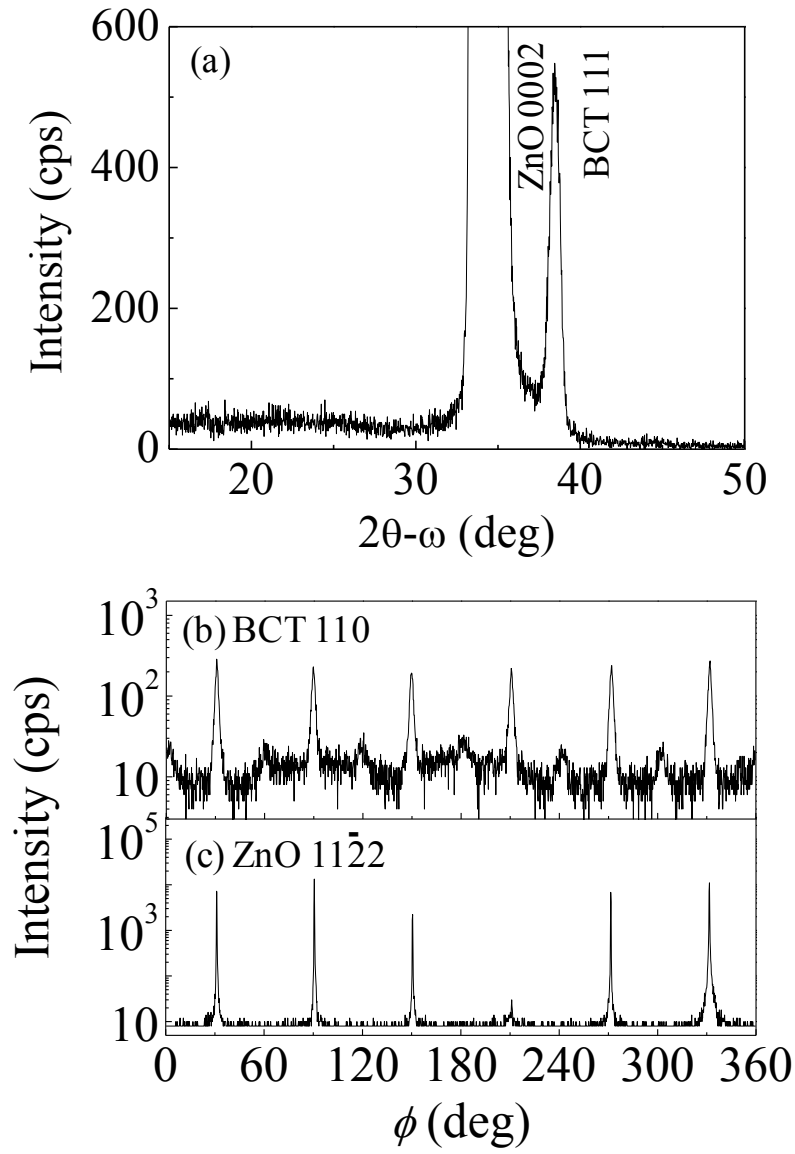


Fig. 5.5 (a) XRD 2θ-ω profile of BCT films deposited on the reconstructed surface. The XRD ϕ scan are also shown for (b) the BCT 110 and (c) the ZnO 11̄22 reflections.

originate from oxygen vacancies at the oxygen-terminated surface [14, 15]. This atomic arrangement in ZnO surface should help (111) growth of BCT through reduction of the number of dangling bonds, ordering of the lattice length, and change in the interface charges. The interface energy at the heterointerface is determined by the surface energies of BCT and ZnO and by the adhesion energy between BCT and ZnO [12, 16, 17]. These surface and adhesion energies depend on the crystal orientation and the interface bond density, respectively. The surface energy of (111) BTO (7.3–8.4 eV) is reported to be considerably larger than that of (001) BTO (1.1–1.5 eV) [18–20]. Therefore, the adhesion energy of (111) BCT to ZnO should be higher than that of (001) BCT. The reconstructed surface has fewer dangling bonds because of the formation of dimer or trimer structures [21–23]. Therefore, the adhesion energy of the ZnO surface is reduced on the reconstructed surface. In addition, the dangling bond density of the Ti-O covalent bonds at the Ti plane of the (111) BCT surface ($1.1 \times 10^{15} \text{ cm}^{-2}$) is larger than that at the TiO_2 plane of the (001) BCT surface ($6.3 \times 10^{14} \text{ cm}^{-2}$). Thus, the surface reconstruction seems to increase the bond density mismatch between (111) BCT and ZnO. As mentioned earlier, the (111) BCT grown on the reconstructed ZnO has 30° rotated domains. The (111) BCT with the epitaxial relationship of $[110]\text{BCT} \parallel [10\bar{1}0]\text{ZnO}$ matches the ZnO lattice, as shown at the bottom of Fig. 5.6(a). The domain with $[112]\text{BCT} \parallel [10\bar{1}0]\text{ZnO}$ shows larger lattice mismatches of more than -12% , as shown at the top of Fig. 5.6(a). The existence of the (111) BCT with $[112]\text{BCT} \parallel [10\bar{1}0]\text{ZnO}$, which has high bond density at the heterointerface, indicates that the adhesion energy has little effect on BCT growth.

The polar discontinuity should also be taken into account at this heterointerface, because both the $(000\bar{1})$ ZnO and (111) BCT faces exhibit polar surfaces. The (111)

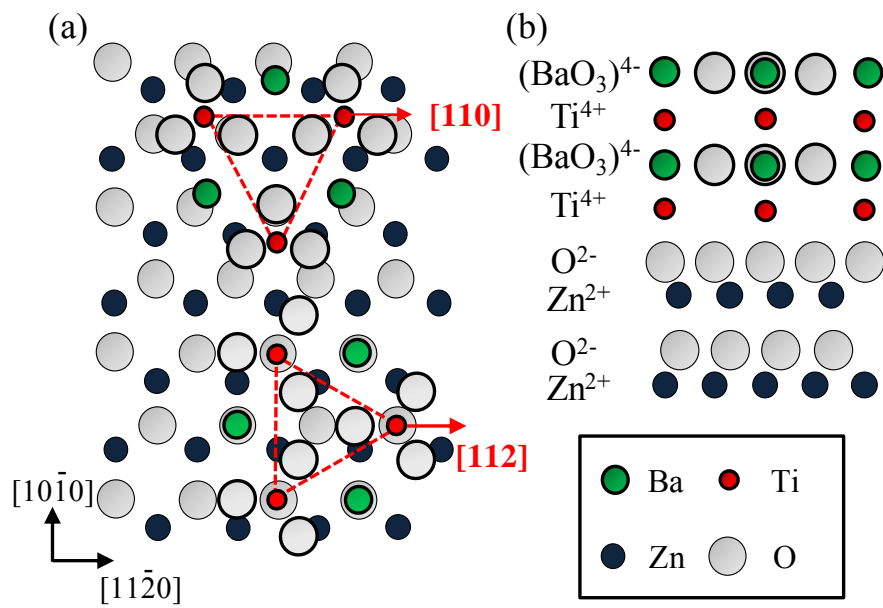


Fig. 5.6 Schematics of (a) the top and (b) the cross-sectional view of the atom arrangements of the interfaces between (111) BCT and (000 $\bar{1}$) ZnO.

plane of BCT can be formally divided into $(\text{Ba,Ca})\text{O}_3^{4-}$ and Ti^{4+} layers, while the $(000\bar{1})$ ZnO surface consists of an O^{2-} layer that includes three oxygen atoms in the corresponding area, as shown in Fig. 5.6(b). This interface has a formal charge difference of around -2 electrons per unit cell. Without a neutralization process such as a rearrangement of the atoms, the electrostatic potentials that will be generated perpendicular to the interface are greater than the band gaps of the materials. It is obvious that such large potentials cannot be sustained in real systems. Many reports propose mechanisms to prevent generation of this large potential, such as redistribution of the electrons and ions like an oxygen vacancy, intermixing of the atoms, and screening by a metallic buffer layer [24–27]. Electron and ion redistribution was reported at two insulator interfaces of $\text{LaAlO}_3/\text{SrTiO}_3$ [24]. The n-type interface with $(\text{LaO})^+/(\text{TiO}_2)^0$, which exhibits a metal-insulator transition, is formed by electron redistribution, while the p-type interface with $(\text{AlO}_2)^-/(\text{SrO})^0$, which has an insulating nature, is compensated by ions. Harrison et al. reported the interface formation of polar and non-polar heterojunctions of GaAs/Ge [25]. In this case, the rearrangement of the atoms or the formation of the dangling bonds occurred because of the covalent bonding features of the materials rather than the movement of the electrons. Both systems can be applied to the BCT/ZnO system because of the iconicity of ZnO, which resides on the borderline between ionic and covalent bonding natures. In the case of the former mechanism, the role of the reconstructed surface should be to provide interface charges to compensate for the charge mismatch, similar to the p-type interface of $\text{LaAlO}_3/\text{SrTiO}_3$. The oxygen vacancy, which is believed to be the origin of the $(\sqrt{3} \times \sqrt{3})\text{R}30^\circ$ reconstructed surface, can form interface charges, but can also form the dangling bonds of Zn. It therefore seems that the interface behavior cannot be accounted for by the former mechanism alone. In the case of the latter mechanism, the zig-zag-shaped surface and its

structural arrangement reduces the electrostatic potentials, similar to the atomic rearrangement in the GaAs/Ge systems. Additionally, the (111) faces of perovskite oxides are experimentally formed with mixed terminations, although a few reports revealed single terminations at the (111) surfaces [28–30]. The grain growth with two in-plane epitaxial relationships, which is revealed by the combination of RHEED and XRD, also suggests mixed termination of the BCT film. If the ionic charges of the oxygen vacancies are the main reason for the interface charge compensation, then a single termination with Ti is desirable because of the uniform and negatively charged surface of ZnO with O termination, while the structural arrangement allows mixed termination at the initial growth stage. It is therefore proposed that charge matching at the heterointerfaces through the structural arrangement with the surface oxygen vacancies may be the reason for the (111) growth of BCT films on the reconstructed ZnO surface.

5.4 Conclusions

The heteroepitaxial growth of BCT thin films on ZnO substrates was investigated. The (111) BCT thin films were epitaxially grown on ZnO using the $(\sqrt{3} \times \sqrt{3})R30^\circ$ reconstructed surfaces, while only (001)-oriented BCT films were obtained on (1×1) ZnO surfaces. The (111) BCT thin films were grown epitaxially with a small lattice misfit on $(000\bar{1})$ ZnO, although small numbers of the 30° -rotated grains existed. The (111)-growth of the BCT thin films on reconstructed ZnO was possibly caused by the reduction of the interface charges at the heterointerface through the atomic rearrangements.

References

- [1] V. Vaithyanathan, J. Lettieri, W. Tian, A. Sharan, A. Vasudevarao, Y. L. Li, A. Kochhar, H. Ma, J. Levy, P. Zschack, J. C. Woicik, L. Q. Chen, V. Gopalan, and D. G. Schlom, J. Appl. Phys. **100**, 024108 (2006).
- [2] R. A. McKee, F. J. Walker, and M. F. Chisholm, Phys. Rev. Lett. **81**, 3014 (1998).
- [3] R. C-. Guerrero, J. P. Veazey, J. Levy, and R. Droopad, Appl. Phys. Lett. **102**, 012907 (2013).
- [4] W. B. Luo, J. Zhu, H. Chen, X. P. Wang, Y. Zhang, and Y. R. Li, J. Appl. Phys. **106**, 104120 (2009).
- [5] T. Yamada, P. Murali, V. O. Sherman, C. S. Sandu, and N. Setter, Appl. Phys. Lett. **90**, 142911 (2007).
- [6] Y. Kato, Y. Kaneko, H. Tanaka, and Y. Shimada, Jpn. J. Appl. Phys. **47**, 2719 (2008).
- [7] D. Fu, M. Itoh, and S. Koshihara, J. Phys.: Condens. Matter **22**, 052204 (2010).
- [8] S. Suzuki, A. Honda, S. Higai, A. Ando, N. Wada, and H. Takagi, Jpn. J. Appl. Phys. **50**, 09NC11 (2011).
- [9] I. Levin, V. Krayzman, and J. C. Woicik, Appl. Phys. Lett. **102**, 162906 (2013).
- [10] W. Cao, S. Bhaskar, J. Li, and S. K. Dey, Thin Solid Films **484**, 154 (2005).
- [11] W. Tian, V. Vaithyanathan, D. G. Schlom, Q. Zhan, S. Y. Yang, Y. H. Chu, and R. Ramesh, Appl. Phys. Lett. **90**, 172908 (2007).
- [12] X. H. Wei, Y. R. Li, W. J. Jie, J. L. Tang, H. Z. Zeng, W. Huang, Y. Zhang, and J. Zhu, J. Phys. D: Appl. Phys. **40**, 7502 (2007).
- [13] H. V. Hove and R. Leyser, Phys. Stat. Sol. (a) **9**, 361 (1972).
- [14] S. T. King, S. S. Parihar, K. Pradhan, H. T. J-. Steigelman, P. F. Lyman, Surf. Sci. Lett. **602**, L131 (2008).
- [15] J. M. Li, C. Li, F. Wang, A. Sun, and Y. Jia, Mod. Phys. Lett. B **24**, 2803 (2010).

- [16] K. Hirama, Y. Taniyasu, and M. Kasu, J. Appl. Phys. **108**, 013528 (2010).
- [17] C. H. Jia, Y. H. Chen, B. Zhang, X. L. Liu, S. Y. Yang, W. F. Zhang, and Z. G. Wang, Appl. Surf. Sci. **258**, 2927 (2012).
- [18] R. I. Eglitis, Phase Trans. **86**, 1115 (2013).
- [19] E. Heifets, E. A. Kotomin, and J. Maier, Surf. Sci. **462**, 19 (2000).
- [20] R. I. Eglitis and D. Vanderbilt, Phys. Rev. B **76**, 155439 (2007).
- [21] D. J. Chadi, Phys. Rev. Lett. **43**, 43 (1979).
- [22] D. Loretto, J. M. Gibson, and S. M. Yalisove, Phys. Rev. Lett. **63**, 298 (1989).
- [23] P. Kruger and J. Pollmann, Phys. Rev. Lett. **74**, 1155 (1995).
- [24] N. Nakagawa, H. Y. Hwang, and D. A. Muller, Nature Mater. **5**, 204 (2006).
- [25] W. A. Harrison, E. A. Kraut, J. R. Waldrop, and R. W. Grant, Phys. Rev. B **18**, 4402 (1978).
- [26] J. L. Blok, X. Wan, G. Koster, D. H. A. Blank, and G. Rijnders, Appl. Phys. Lett. **99**, 151917 (2011).
- [27] J. C. Chang, J. -W. Lee, and S. -K. Kim, J. Cryst. Growth, **312**, 612 (2010).
- [28] H. Tanaka and T. Kawai, Surf. Sci **365**, 437 (1996).
- [29] J. Chang, Y. -S. Park, and S. -K. Kim, Appl. Phys. Lett. **92**, 152910 (2008).
- [30] J. Chang, Y. -S. Park, J. -W. Lee, and S. -K. Kim, J. Cryst. Growth **311**, 3771 (2009).

Chapter 6: Summary

The thesis has been devoted to the study of the field-effect of spontaneous polarizations on the ferroelectric/polar semiconductor heterostructures. The main results in this work are summarized in this chapter.

In chapter 2, the ferroelectric/polar semiconductor heterostructures with YbMnO_3 and ZnO were fabricated and the electronic transport properties of the heterostructures are investigated using the Hall-effect measurements at temperatures ranging from 80 to 300 K. Based on the results obtained, it was found that both the carrier concentration and the mobility of the ZnO channel decreased after the deposition of YbMnO_3 . The electron scattering mechanisms of ZnO thin films and $\text{YbMnO}_3/\text{ZnO}$ heterostructures were analyzed using various scattering mechanisms. The results indicate that changes in the electronic transport properties in the ZnO layer were caused by changes in the dominant scattering factor from the grain boundary to the ionized impurity scattering. Thus, it is proposed that ferroelectric domains, which exist in the YbMnO_3 layer, degrade the electron transports through the partially depleted region in the ZnO channels.

In chapter 3, the electronic transport properties in CP-type FeFETs with P(VDF-TeFE)/ZnO heterostructures were characterized using Hall-effect measurements. The FeFETs showed a large ON/OFF ratio exceeding 10^5 , which was caused by the optimization of the fabrication conditions. From the Hall-effect measurements, it was indicated that ferroelectric polarization modulates not only the carrier concentration, but also the mobility, especially close to the interfaces. The multidomain structure of the ferroelectric layer may be responsible for the decreased mobility. Therefore, the ferroelectric layer needs to be fully polarized to enable the use of devices such as FETs and

HEMTs. The origin of the mobility enhancements that were caused by ferroelectric polarization was discussed using the conventional scattering mechanisms of semiconductors. The results showed that ferroelectric polarization enhances the mobility by reducing ionized impurity scattering that is caused by screening of the Coulomb potential.

In chapter 4, the effect of the spontaneous polarization of ZnO on the electrical properties of P(VDF-TrFE)/ZnO heterostructures was discussed. Both P(VDF-TrFE)/O- and Zn-polar ZnO heterostructures show typical electrical characteristics of MFS structures. Moreover, significant differences were observed in the depletion behavior. While the P(VDF-TrFE)/O-polar ZnO exhibits clear depletion behavior, heterostructures with Zn-polar ZnO are weakly depleted. To investigate the origin, the band alignments of the heterostructures were revealed by performing XPS measurements. The results indicated that both heterostructures form a staggered band configuration with a large E_{VBO} that ranges from 2.7–2.9 eV. It was concluded that the effect of spontaneous polarization on the electrical properties appears via carrier generation because of the charge neutralization at the interface and a large E_{VBO} .

In chapter 5, the heteroepitaxial growth of BCT thin films on ZnO substrates was investigated. While growth with an epitaxial relationship of $(111)[110]\text{BCT} \parallel (000\bar{1})[10\bar{1}0]\text{ZnO}$ is expected because of the good lattice matching between the materials, (111) BCT thin films were not obtained on ZnO. The $(\sqrt{3} \times \sqrt{3})\text{R}30^\circ$ reconstructed ZnO surface was focused to reduce the interface formation energy between (111) BCT and $(000\bar{1})\text{ZnO}$. As a result, (111) BCT thin films were successfully grown on the reconstructed ZnO surface. It was also shown that while the epitaxial relationship of $[110]\text{BCT} \parallel [10\bar{1}0]\text{ZnO}$ is

dominant, there is a small quantity of $[112]\text{BCT}||[10\bar{1}0]\text{ZnO}$. The results indicate that the (111)-growth of BCT thin films on reconstructed ZnO may be responsible for the reduction of the interface charges at the heterointerface through the atomic rearrangements.

The results described here indicate that based on the nature of spontaneous polarization, ferroelectrics can positively contribute to electron transport through the field-effect, and polar semiconductors affect the electrical properties depending on the polarization. Therefore, the applicability of the heterointerfaces of ferroelectric and polar semiconductors for novel electronic device is revealed.

Acknowledgements

I owe many thanks to many people for this work, foremost Professor Norifumi Fujimura. I am also grateful to Professor Hiroyoshi Naito and Professor Seiji Akita for their useful advises and reviewing this thesis.

I would like to express my deepest gratitude to Associate Professor Takeshi Yoshimura for the assiduous discussions and the firm guidance. I would like to thank to Associate Professor Atsushi Ashida for the advisements to my research.

The part of this work has been performed under the approval of the Photon Factory Program Advisory Committee (Proposal numbers 2011G638, 2013G185, and 2013G617). I gratefully acknowledge the High Energy Accelerator Research Organization. I also appreciate Professor Toshiyuki Matsui and Ryoichi Shinoda for variable advisement about the XPS measurements and the analysis.

This work was supported by the Grant-in-Aid for Japan Society for the Promotion of Science Fellows (grant number 25-10998).

I would like to acknowledge to Dr. Keiichiro Masuko, Dr. Tadahiro Fukushima, Dr. Kazuhiro Maeda, Dr. Tatsuru Nakamura, Mr. Yuhei Nomura, and Mr. Tomoya Komae for the cooperation in the present research and thank to the members of the Physic of Novel Device Research group.

Finally, I need to thank my parents, brother, and sister for their constant supports and encouragements.

Original Articles Regarding This Thesis

No.	Title	Authors	Journal	Related section
1	Electronic Transport Property of a YbMnO ₃ /ZnO Heterostructure	H. Yamada, T. Fukushima, T. Yoshimura, N. Fujimura	Journal of the Korean Physical Society, Vol. 58, pp. 792 – 796 (2011).	Chapter 2
2	Effect of Ferroelectric Polarization Domain Structure on Electronic Transport Property of Ferroelectric/ZnO Heterostructure	H. Yamada, T. Fukushima, T. Yoshimura, N. Fujimura	Japanese Journal of Applied Physics, Vol. 50, pp. 09NA06-1 – 09NA06-4 (2011).	Chapter 3
3	Electronic Transport in Organic Ferroelectric Gate Field-Effect Transistors with ZnO Channel	H. Yamada, T. Yoshimura, N. Fujimura	Materials Research Society Symposium Proceedings, Vol. 1430, pp. mrss12-1430-e04-08 (2012). (San Francisco, USA, 2012)	Chapter 3
4	Effect of Ferroelectric Polarization on Carrier Transport in Controlled Polarization Type Ferroelectric Gate Field-Effect Transistors with Poly(vinylidene fluoride -tetrafluoroethylene)/ ZnO Heterostructure	H. Yamada, T. Yoshimura, N. Fujimura	Japanese Journal of Applied Physics, Vol. 51, pp. 11PB01 – 11PB04 (2012).	Chapter 3
5	Effects of Polarization of Polar Semiconductor on Electrical Properties of Poly(vinylidene fluoride -trifluoroethylene)/ ZnO Heterostructures	H. Yamada, T. Yoshimura, N. Fujimura	Journal of Applied Physics, submitted.	Chapter 4
6	Epitaxial Growth of (111) (Ba _{0.9} Ca _{0.1})TiO ₃ Thin Films on (000 $\bar{1}$) ZnO	H. Yamada, T. Yoshimura, N. Fujimura	Journal of Crystal Growth, submitted.	Chapter 5